

η Carinae: high angular resolution continuum, H30 α and He30 α ALMA images

Zulema Abraham,^{1*} Pedro. P. B. Beaklini,^{1,2} Pierre Cox,³ Diego Falceta-Gonçalves⁴
and Lars-Åke Nyman⁵

¹*Instituto de Astronomia, Geofísica e Ciências Atmosféricas, Universidade de São Paulo
Rua do Matão 1226, CEP 05508-090, São Paulo, Brazil*

²*National Radio Astronomy Observatory, 1003 Lopezville Road, Socorro, NM 87801, USA*

³*Institut d'Astrophysique de Paris, Sorbonne Université, UPMC Université Paris 6 and CNRS,
UMR 7095, 98bis boulevard Arago, 75014, Paris, France*

⁴*Escola de Artes, Ciências e Humanidades, Universidade de São Paulo,
Rua Arlindo Bettio 1000, CEP 03828-000, São Paulo, Brazil*

⁵*European Southern Observatory, Alonso de Córdoba 3107, Vitacura, Chile*

Accepted XXX. Received YYY; in original form ZZZ

ABSTRACT

We present images of η Carinae in the recombination lines H30 α and He30 α and the underlying continuum with 50 mas resolution (110 AU), obtained with ALMA. For the first time, the 230 GHz continuum image is resolved into a compact core, coincident with the binary system position, and a weaker extended structure to the NW of the compact source. Iso-velocity images of the H30 α recombination line show at least 16 unresolved sources with velocities between -30 and -65 km s⁻¹ distributed within the continuum source. A NLTE model, with density and temperature of the order 10⁷ cm⁻³ and 10⁴ K, reproduce both the observed H30 α line profiles and their underlying continuum flux densities. Three of these sources are identified with Weigelt blobs D, C and B; estimating their proper motions, we derive ejection times (in years) of 1952.6, 1957.1, and 1967.6, respectively, all of which are close to periastron passage. Weaker H30 α line emission is detected at higher positive and negative velocities, extending in the direction of the Homunculus axis. The He30 α recombination line is also detected with the same velocity of the narrow H30 α line. Finally, the close resemblance of the H30 α image with that of an emission line that was reported in the literature as HCO⁺(4-3) led us to identify this line as H40 δ instead, an identification that is further supported by modeling results. Future observations will enable to determine the proper motions of all the compact sources discovered in the new high-angular resolution data of η Carinae.

Key words: circumstellar matter: masers – stars: individual (Eta Carinae) – stars: mass loss – stars: winds, outflows

1 INTRODUCTION

The massive ($M \gtrsim 120 M_{\odot}$) and highly eccentric ($e \sim 0.9$) binary system formed by η Carinae (hereafter η Car) and its unknown companion (Damineli 1996; Davidson & Humphreys 1997; Corcoran et al. 2001; Falceta-Gonçalves, Jatenco-Pereira & Abraham 2005) attracted the astronomers' attention after the ejection of a large amount of matter ($\gtrsim 12 M_{\odot}$) in a dramatic eruption that started around 1840 and formed what it is now known as the Homunculus Nebula, which expands with a velocity of about 650 km s⁻¹ (Gaviola 1950; Smith et al. 2003a). This event characterized η Car as a probable Luminous Blue Variable (LBV) star: its brightness increased abruptly by about four magnitudes and decreased steadily

by nine magnitudes in 20 years, as dust formed and absorbed the visible light, re-emitting it in the infrared (Humphreys, Davidson & Smith 1999).

Another smaller eruption occurred in 1887, also characterized by a sudden increase in brightness that lasted for seven years (Humphreys et al. 1999), forming the Little Homunculus, detected inside the Homunculus at a distance of about 2 arcsec from the binary system, and expanding with a velocity of about 200 km s⁻¹ (Ishibashi et al. 2003).

A third, small and sudden increase in luminosity was observed around 1940, but instead of returning to its previous value, the luminosity continued to slowly increase (Humphreys et al. 1999). This event coincided with the first detection of the spectroscopic events (Gaviola 1953), in which high excitation lines disappear from the spectrum for a short time during each binary orbit. Observations of η

* E-mail: zulema.abraham@iag.usp.br

Car obtained with the Atacama Large Millimeter Array (ALMA) in the continuum and various recombination lines led to the discovery of an unresolved cloud of high density ionized gas, whose dynamics correspond to matter ejected during the 1941 event and was therefore named "Baby Homunculus" (Abraham, Falceta-Gonçalves & Beaklini 2014, hereafter Paper I).

Besides those isolated episodes of mass ejection, η Car loses mass continuously through a massive wind, with a mass loss rate $\dot{M} \sim 10^{-3} M_{\odot} \text{ yr}^{-1}$ and a velocity $v \sim 500 \text{ km s}^{-1}$ (Groh et al. 2012). The companion star, although undetected, must also be losing mass through a less massive but faster wind ($\dot{M} \sim 10^{-5} M_{\odot} \text{ yr}^{-1}$, $v \sim 3000 \text{ km s}^{-1}$), in order to explain the observed X-ray emission arising from hot shocked material in the wind-wind collision zone (Corcoran et al. 2001).

The combination and superposition of all these processes complicate the interpretation of the images and spectra of η Car and its surroundings, in addition to the variability with orbital phase and along the binary cycles.

Observations at UV and optical wavelengths show a series of broad emission lines, sometimes with P Cygni absorption profiles (Gull et al. 2005; Nielsen, Gull & Kober 2005; Gull, Kober & Nielsen 2006; Martin et al. 2010), as well as narrow emission lines, some of them from high excitation states (Davidson et al. 1997; Morse et al. 1998; Gull et al. 2009; Mehner et al. 2010; Gull et al. 2016). Those include the so-called Weigelt blobs, which are dense condensation of matter ($n_e \sim 10^7 \text{ cm}^{-3}$, $T_e \sim 10^4 \text{ K}$), discovered in 1986 at distances of $0''.1 - 0''.3$ from the binary system (Weigelt & Ebersberger 1986) that are moving away with velocities of several mas yr^{-1} (Hofmann & Weigelt 1988; Davidson et al. 1997; Smith et al. 2004; Dorland, Currie & Hajian 2004).

Infrared images reveal a complex dust distribution around η Car, implying that some of the UV and optical structures could be the result of selective absorption (Morris et al. 1999; Hony et al. 2001; Chesneau et al. 2005; Artigau, Martin & Humphreys 2011; Morris et al. 2017).

The properties of the individual stars in the binary system are only inferred from indirect observations. The mass of η Car, according to the Eddington limit, should be larger than $120 M_{\odot}$. Its mass loss rate is very large and its photosphere cannot be observed directly, but a possible range of effective temperatures was calculated fitting its spectra to models obtained from a non LTE-line blanketed code (Hillier et al. 2001, 2006). Using the observed present bolometric luminosity of $5 \times 10^6 L_{\odot}$, inferred from the total emission of the Homunculus Nebula at a distance of 2.3 kpc, and the mass loss rate and terminal velocity mentioned before, they found an effective temperature $T_{\text{eff}} \sim 30,000 \text{ K}$, which gives a stellar radius of $R \sim 60 R_{\odot}$ and a rate of ionizing photons provided by the star of $Q \sim 2 \times 10^{50} \text{ ph s}^{-1}$.

The spectra of the companion star is not detected, but its effective temperature was estimated from the number of ionizing photons with energies larger than 40 eV, necessary to account for the observed high ionization lines in the Weigelt blobs. Fitting radiative transfer models to the high ionization spectra of the blobs Verner, Bruhweiler & Gull (2005) and Mehner et al. (2010) showed that their electron densities should be $\sim 10^6 - 10^7 \text{ cm}^{-3}$ and the rate of Lyman ionizing photons from the secondary star $Q \sim 10^{49} \text{ ph s}^{-1}$, corresponding to effective temperatures of $\sim 37,000 - 40,000 \text{ K}$. Depending on the evolutionary state (main sequence, supergiant or Wolf-Rayet), the mass of the companion star should be $\sim 30 - 40 M_{\odot}$.

Numerical simulations of the wind-wind collision in a region centered on η Car and extending up to 100 times the semi-major

axis of the binary orbit show a series of dense ($n_e \sim 10^7 \text{ cm}^{-3}$) arc-like features formed by both the colliding winds and the winds ejected in the previous cycles (Parkin, et al. 2011; Clementel et al. 2014; Russell et al. 2016) that are in good agreement with observed optical images (Gull et al. 2016).

Radio frequencies are powerful tools for studying the matter distribution in the surroundings of η Car, since they are not absorbed by dust. Continuum and recombination line H91 α and H106 α images with arcsec resolution were obtained since 1992 with the Australian Compact Array (ATCA) at 3 and 6 cm, revealing a compact source, coincident with the central star and extended emission distributed around it with structures that changed with orbital phase (White et al. 1994; Duncan et al. 1995; Duncan, White & Lim 1997; Duncan & White 2003). A non-resolved component centered at the star position was observed in the continuum and recombination lines during periastron passage, which evolved at apastron into an elongate $4''$ long ridge in the NE-SW direction, with a central velocity close to the star velocity and half power width (HPW) of 500 km s^{-1} . In addition, a compact component in the NW direction at a distance of $1''.2$ from the star was reported, with a velocity of -286 km s^{-1} and HPW of 250 km s^{-1} , and is related to the Little Homunculus (Smith 2005; Teodoro et al. 2008).

Single dish continuum observations at 1.3 and 2.9 mm with $30''$ and $50''$ resolution, respectively, showed a compact, non-resolved source, with orbital phase dependent flux density that increased with frequency (Cox et al. 1995a). H40 α , H30 α and H29 α recombination lines were also observed, presenting strong and narrow profiles, with velocities centered at -50 km s^{-1} , revealing the existence of ionized gas in NLTE, with electron density of about 10^7 cm^{-3} (Cox et al. 1995b).

The surroundings of η Car were further observed using ALMA in CO and HCN emission lines revealing a cool, disrupted equatorial torus located 4000 AU (corresponding to $1''.8$) from the star (Smith, Ginsburg & Bally 2018). Bordiu & Rizzo (2019) also reported an extended structure northwest of η Car seen in the continuum and in only one emission line, that they identified with HCO⁺(4-3).

Previous continuum observations of the central region of η Car with ALMA were done in Cycle 0, with frequencies and resolutions ranging from 100 – 700 GHz and $3'' - 0''.4$, respectively, and revealed a spectrum characteristic of compact H II regions, with a turnover frequency around 300 GHz (Paper I). Strong narrow hydrogen recombination lines (H42 α , H40 α , H30 α , H28 α and H21 α), with central velocities of $\sim -55 \text{ km s}^{-1}$ and HPW of $\sim 40 \text{ km s}^{-1}$ were also detected, showing departure from LTE condition. Neither the continuum nor the recombination line images were resolved in these observations, even at the highest frequencies.

In this paper, we present new ALMA observations with an order of magnitude higher resolution ($0''.065 \times 0''.043$) than in previous observations, obtained in the continuum and in the recombination lines of H30 α and He30 α . The new data reveal 16 individual unresolved components with different velocities, three of which are identified with Weigelt blobs B, C and D. The paper is organised as follows: in Section 2, we describe the observations; in Section 3, we present the results; in Section 4, we discuss and analyze the main results; and, in Section 5, we outline the conclusions of this study.

In the paper, we assume that η Car¹ is at a distance of 2300 pc (Davidson et al. 1997), so that 0.1 arcsec corresponds to 224 AU. Over the 5.54 year orbital period, 100 km s^{-1} corresponds to

¹ The ICRS coordinates of η Car are: $\alpha(\text{J2000}) = 10:45:3.5362$, $\delta(\text{J2000}) = -59:41:4.0534$

a spatial motion of 110 AU or 50 mas on the plane of the sky. All the velocities are referred to the Local Standard of Rest (LSR); in the direction of η Car, the difference between LSR and heliocentric velocity is -11.6 km s^{-1} ; in the LSR, the velocity of η Car is -19.7 km s^{-1} (Smith et al. 2004).

2 OBSERVATIONS

The observations were performed in November 20, 2017 with ALMA band 6 receivers, using 43 antennas of the 12 m array, as part of Cycle 5 program 2017.1.00725.S. The closest baseline was 97.1 m, constraining the maximum recovery scale to $0''.8$, while the largest baseline was 8457.6 m, resulting in an angular resolution of 50 mas. The total observation time was 30 minutes, of which 13 minutes were on the source. The data is divided into 4 spectral windows, the main one centered at the frequency of the H30 α recombination line (231.900 GHz) and the others, focused on the continuum emission, centered at 230.519, 218.018, and 215.518 GHz. The line spectral window has 1.875 GHz bandwidth, with channel width resolution of 976 kHz, producing a datacube of 1920 channels. The continuum bands have a bandwidth of 2 GHz divided into 128 channels. The pointing, focusing, amplitude, and flux calibration were performed through observations of the quasar J0904-5735, while quasar J1032-5917 was the phase calibrator. Data were processed using the CASA 5.4.0 version.

The continuum image was obtained using the continuum bands plus the channels of the main spectral window where the line is not present. The spectral cube was obtained for the spectral window of the recombination line after continuum subtraction. The convolution method used the Hogbom algorithm with Briggs weighting. The synthesized beam has a major axis of 65 mas and minor axis of 43 mas for both continuum and emission line images, and for both cases, the images have a cell size of 0.1 mas and a total size of 2048×2048 pixels. In velocity, the cube range goes from -1187 to 1235 km s^{-1} , with a velocity resolution of 1.262 km s^{-1} .

3 RESULTS

3.1 Continuum emission

Figure 1 presents the 230 GHz continuum image of the $0''.8 \times 0''.8$ (1800 AU) central region of η Car. It shows a strong compact component, coincident in position with the binary system, and emission extending north-west of the compact source.

The integrated 230 GHz continuum flux density of the observed region is $28.3 \pm 0.1 \text{ Jy}$. The compact source HPW is $0''.13 \times 0''.11$, in the directions of the major and minor axis of the beam ellipse. Its flux density is $4.5 \pm 0.1 \text{ Jy}$ and although its size is larger than the half power beam width (HPBW), no structure is observed. The extended emission covers about $0''.6$ and appears structured with regions of enhanced emission.

Previous ALMA continuum imaging results at 346 GHz, published by Bordiu & Rizzo (2019), already showed a similar structure with a point-like source and an extended emission in the north-west direction (which they labeled "Peanut"), although these data were taken at a lower angular resolution ($0''.17 \times 0''.13$) and signal-to-noise ratio.

Comparison of the integrated continuum emission with previous observations must take into account orbital phase and cycle. Considering the binary period of 2024 days and the date 2014 July 1 (MJD 56850) as phase 13.0 (Damineli et al. 2019; Corcoran et

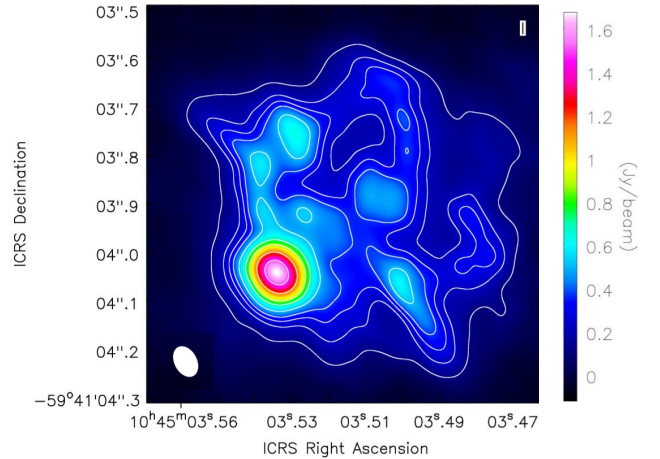


Figure 1. 230 GHz continuum image (raster and contours) of η Car. Contours are 0.1, 0.17, 0.22, 0.27, 0.36, 0.5, 0.6, 0.8 and 1.0 Jy beam^{-1} . The scale of the continuum flux is displayed on the right axis of the panel. The 65×43 mas synthesized beam (angle $24''.5$) is shown in white at the bottom.

al. 2017), our ALMA Cycle 5 observations in 2017 Nov 20 corresponded to phase 13.61 and those of ALMA Cycle 0 (Paper I), obtained in 2012 Nov 4, to phase 12.70. Taking into account the high eccentricity of the binary orbit (~ 0.9), these two phases correspond to similar orbital positions of the companion star, separated from apastron by 3° and 5° , respectively. Therefore, both observations can be directly compared regarding the relative orbital position; the total continuum flux density in the present observation is 32% lower than that detected in 2012, when the source was not resolved by the ALMA $1''.52 \times 0''.75$ beam.

While variability between continuum emission at different binary cycles can be expected, the lower flux density obtained in the present observations can be due to the existence of emission outside the maximum recovery scale of the ALMA configuration. This seemed to be also the case with the ALMA 346 GHz continuum observations obtained by Bordiu & Rizzo (2019) in 2016 October 24. The orbital phase at that time was 13.41 and the secondary orbital position 13° before apastron. The integrated flux density of the image was $30.5 \pm 1.2 \text{ Jy}$, but the value raised to 38.9 Jy , compatible with the flux densities measured in 2012 and reported in Paper I, when a larger area was included in the integration.

Figure 2 (center and bottom right images) shows the position of the 230 GHz continuum source relative to the *HST* Wide Field Planetary Camera image, obtained with the filter F336W, centered at the wavelength of 3342 \AA (Morse et al. 1998). The position of several features described in the literature are indicated in the central image: the "fan" (Morse et al. 1998), the equatorial "skirt" (Smith, Gehrz & Krautter 1998), the "purple haze" (Smith et al. 2004), and the molecular torus (Smith et al. 2018; Bordiu & Rizzo 2019). The bottom image shows that the continuum radio source is located in the central part of the compact ultraviolet continuum source. The upper left part of Figure 2, which will be discussed in Section 4.4, presents the superposition of the 230 GHz contours on the NB_405 narrow filter image, which includes the Br α line, obtained with the VLT Adaptive Optics system NACO (Chesneau et al. 2005). The position of the "Butterfly Nebula" is also indicated in this Figure.

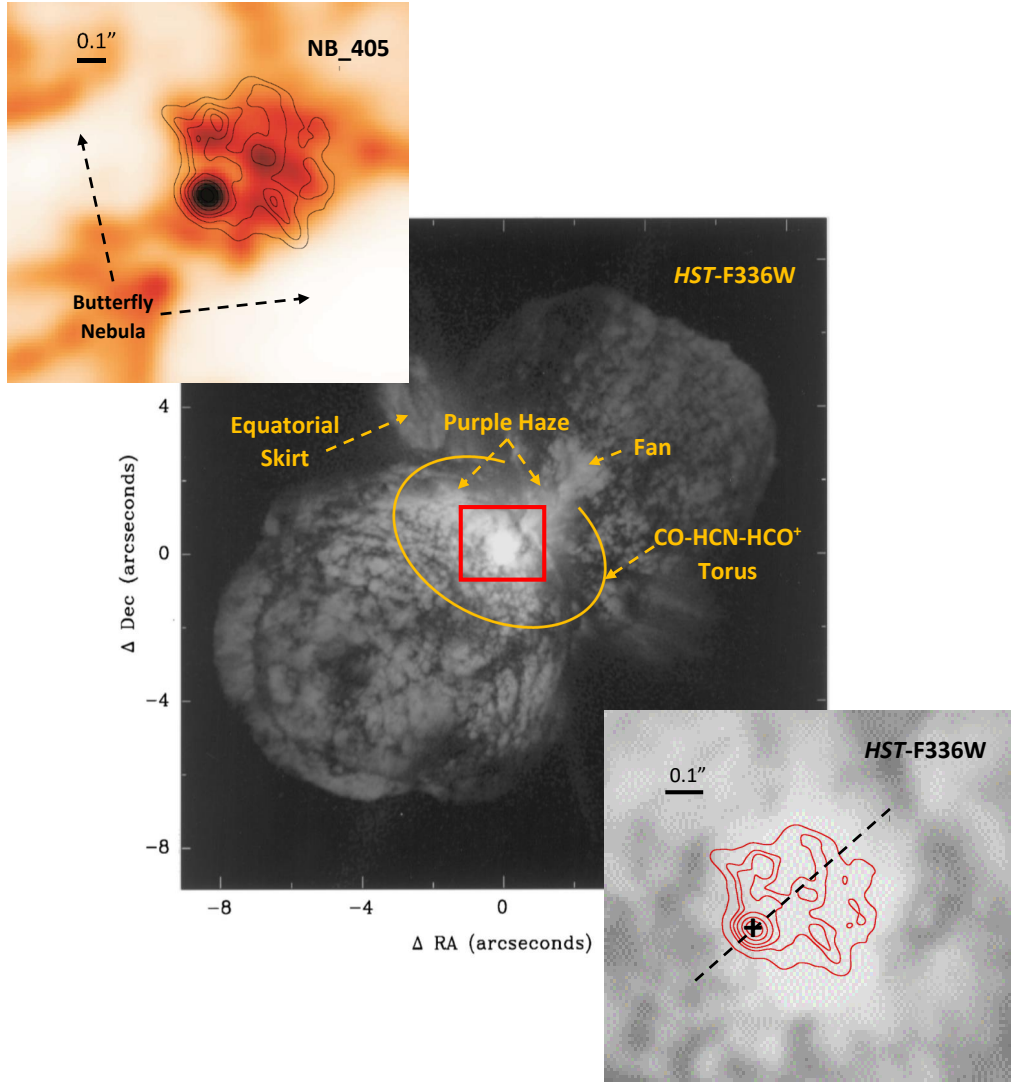


Figure 2. Central image: *HST* Wide Field Planetary Camera image of the Homunculus in the F336W filter (Morse et al. 1998); the red rectangle delimits the size and position of the images in the lower right corner; the main features of the nebula are identified. Bottom right image: 230 GHz continuum contours superimposed to the *HST* image; the black cross represents the position of η Car and the black broken line shows the direction of the position-velocity PV diagram presented in Figure 3. Upper left image: 230 GHz continuum contours superimposed to the NB_405 narrow filter image, which includes the Br α line, obtained with the VLT Adaptive Optics system NACO (Chesneau et al. 2005)

3.2 The H30 α spectrum

Figure 3 (top panel left) shows the H30 α spectrum, centered at the line LSR frequency with velocity resolution of 1.262 km s $^{-1}$, integrated over the whole continuum emitting region. The central velocity of the narrow line is -57.8 km s $^{-1}$, its maximum flux density 60.4 ± 0.1 Jy and HPW 45 km s $^{-1}$. The central velocity is similar to that observed in 2012 (Paper I), but the flux density is lower by 25% and the line width larger by the same amount. The weak emission extends over several hundred km s $^{-1}$, both at positive and negative velocities.

A weak line with 3.9 ± 0.1 Jy maximum flux density and -176 km s $^{-1}$ central velocity is identified with the He30 α line, separated from H30 α by $\Delta\nu/\nu = 0.000407$ or -122 km s $^{-1}$. Considering this

frequency displacement, the actual velocity of the He atoms is -54 km s $^{-1}$, similar to the velocity of the strong H30 α line.

Figure 3 (top panel right) presents the spectrum of the compact region, centered on η Car and integrated over an area of $0''.09$ radius. The narrow line, with maximum flux density of 2.64 ± 0.01 Jy is also centered at -57.8 km s $^{-1}$, blended with an even weaker line, centered at ~ -100 km s $^{-1}$; the He30 α line is also present in the spectrum, as well as extended emission at larger negative and positive velocities. It is not clear if the narrow line belongs to the compact source or if it only represents the contribution of the superimposed extended NW region.

Figure 3 (bottom) displays the position velocity (PV) diagram of the region, collapsed along a line in the direction of the Homunculus axis (42°), with a width of 10 mas, which includes the position of the compact continuum source. The position of the H30 α

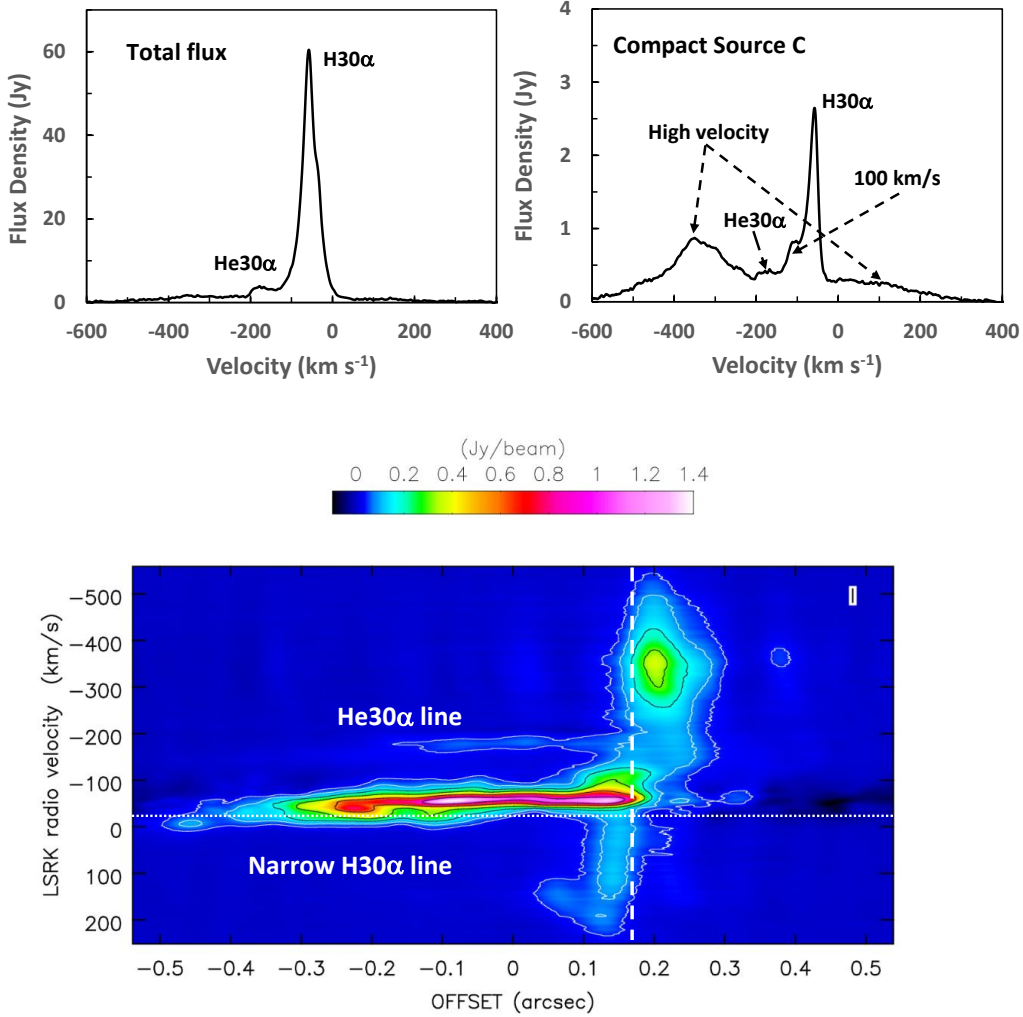


Figure 3. Top left: spectrum of the H30 α line, integrated over the whole continuum emitting region. Top right: spectrum integrated over a circle of 0.09 arcseconds radius, centered on the continuum compact source. Bottom: PV diagram of the region, collapsed along the line shown in the bottom right image of Figure 2, in the direction of the Homunculus axis (42 $^\circ$), with a width of 10 mas, which includes the position of the compact continuum source, shown as a vertical broken line. The horizontal dotted line at -19.7 km s $^{-1}$ represents the LSR velocity of η Car.

Contours are: 0.03, 0.06 (white), 0.12, 0.22, 0.4 and 0.7 (black) of 1.403 Jy beam $^{-1}$

and He30 α lines are clearly visible in the NW direction, as well as the high positive and negative velocity features at both sides of the compact continuum source position.

The LSR velocity of η Car, shown as a dotted horizontal line in Fig. 3, was estimated by Smith (2004) as -19.6 km s $^{-1}$ based on the velocity of the H $_2$ lines in the walls of the expanding Homunculus. This velocity coincides with the -16.1 ± 8.6 km s $^{-1}$ mean velocity of the massive stars in the Tr16 cluster, which includes η Car (Kiminki & Smith 2018). Similar velocities (-15 to -20 km s $^{-1}$) are found in the CO(1 - 0) lines of the Carina Molecular Complex, where Tr16 is located (Rebolledo et al. 2016).

The very good quality of our data enables us to make images for each velocity channel. We separated therefore the H30 α emission in narrow line, high negative and positive velocities, the -100 km s $^{-1}$ line, and extracted images for the He30 α emission line. We discuss the results in the next subsections.

3.3 The strong narrow H30 α line

Figure 4 shows the iso-velocity intensity maps of channels with width of 1.262 km s $^{-1}$, showing the H30 α narrow emission line, superimposed on the 230 GHz continuum emission image. The channels are separated in intervals of about 5 km s $^{-1}$, between -82 and -26 km s $^{-1}$. The line emission at different velocities originates in different regions of the continuum image and the compact source, coincident with η Car, does not contribute to the line emission at these velocities.

Contour maps of the flux density, integrated over the line profile between -25 and -116 km s $^{-1}$ (zero momentum), are presented in Figure 5 (top), superimposed on the the velocity weighted by flux density (first momentum) raster image. The regions of continuum and line enhancement coincide and a velocity gradient in the north-west direction is clearly seen.

The image of the H30 α line at the velocity of maximum emission (-54.6 km s $^{-1}$) is comparable to that of the [Fe III] line at

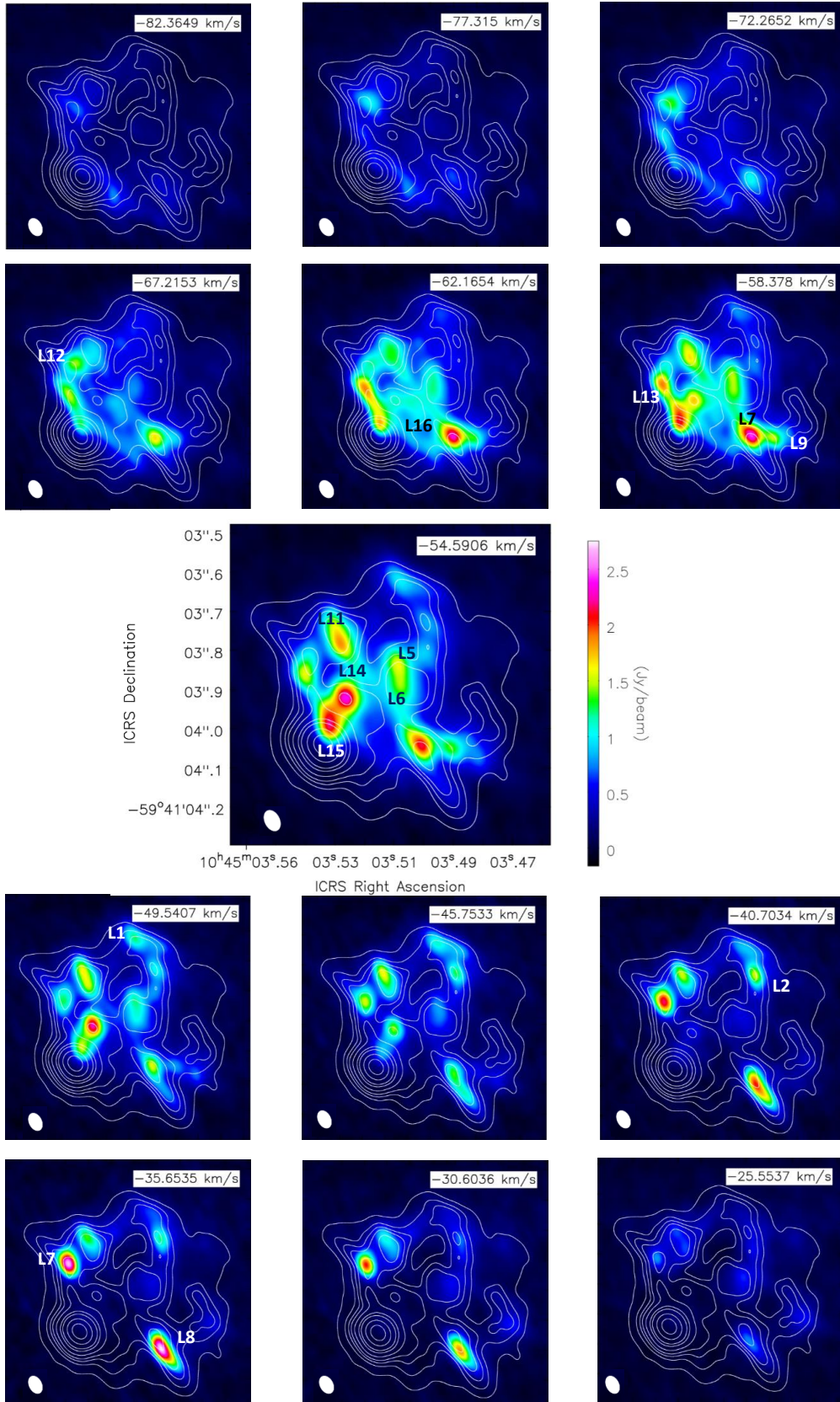


Figure 4. Velocity-integrated intensity maps of channels with width of 1.262 km s^{-1} , showing the H30 α narrow emission line. The channels are separated in intervals of about 5 km s^{-1} , between -82 and -26 km s^{-1} . All the maps have the same intensity scale (shown on the right axis of the middle panel). The center velocities of the H30 α map are indicated in the upper right corners of each panel. The strongest of the compact sources presented in Table 1 (L1, L2, L5 - L9, L11 - L16) are also identified in the images. The H30 α maps are superimposed on the 230 GHz continuum map shown as contours (using the same levels as in Fig. 1)

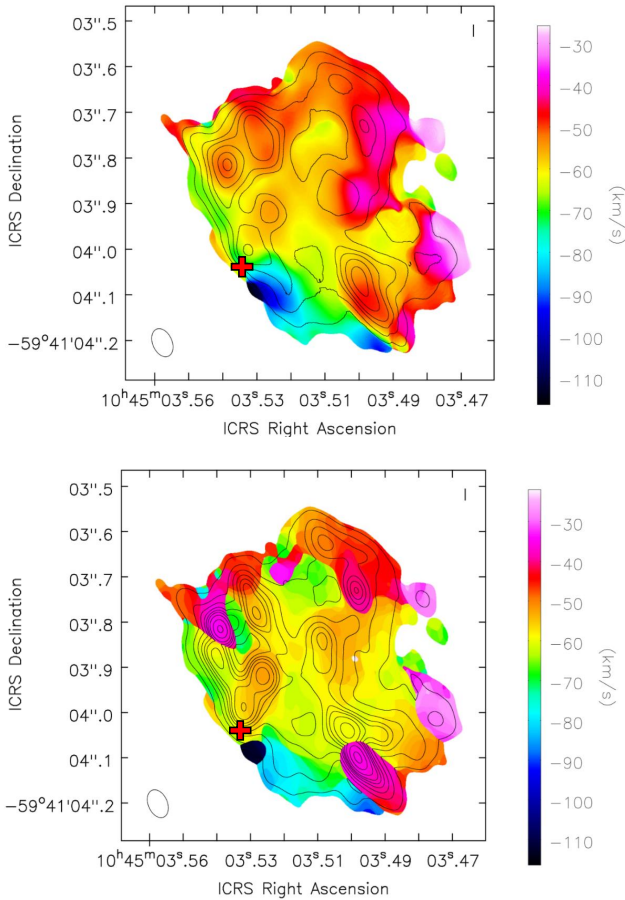


Figure 5. Top image: The zero momentum image of the H30 α recombination line (shown as contours) between -116 and -25 km s $^{-1}$ superimposed on the raster image of the first momentum map. Contours represent 0.1, 0.2, 0.35, 0.45, 0.6, 0.8 and 0.95 of 89.5 Jy beam $^{-1}$ km s $^{-1}$. The red cross represents the position of η Car. Bottom image: The maximum flux density of the H30 α line (contours) superimposed on the raster image of the velocity of the line maximum; contours are 0.1, 0.2, 0.3, 0.4, 0.48, 0.55, 0.65, 0.8 and 0.95 of 2.76 Jy beam $^{-1}$.

similar velocity obtained with the *HST*/STIS, presented by Gull et al. (2016). The authors also reported variations of the optical line velocity with position, although they had less spatial resolution than in our ALMA data (i.e., 0''.1 compared to 50 mas).

More information is obtained from the H30 α line maximum flux density and the velocity of this maximum, which are presented as contours and raster images, respectively, at the bottom of Figure 5. This representation reveals that some of the enhanced emission regions in the zero momentum image are due to compact not resolved components with very different velocities.

We identified sixteen of these individual components, labeled L1 to L16; their spectra, integrated over a region of 66 mas radius are presented in Figure 6. Most of them clearly show the superposition of more than one velocity component.

The absolute position of these sources, continuum and peak flux densities of the H30 α and He30 α lines, peak velocity of each line and HPW of the H line, projected distance D to the compact continuum source and position angle PA are presented in Table 1.

The minimum HPW (17-18 km s $^{-1}$) of the lines that are not blended is of the order of the thermal velocity of a 10 4 K plasma.

Also shown in Table 1 are the emission measures (EM), which will be discussed in Section 4.3. They were calculated from the continuum emission and from the H30 α lines, assuming LTE conditions.

3.4 The He30 α line

Figure 7 presents the He30 α line iso-velocity raster images. The -56.3 km s $^{-1}$ image, which corresponds to a velocity of -178.3 km s $^{-1}$ at the frequency of the H30 α line, agrees very well with the continuum image; the strongest emission arises from compact components coincident with the compact continuum source, but it is not possible to assess if the emission is really part of the He30 α transition or if it corresponds to the H30 α transition with high negative velocity.

The detection of He30 α recombination lines coincident in position and velocity with both the continuum and narrow H30 α line extended source confirms the presence of an ionizing star of spectral type O or Of/WN7, with temperature of $\sim 37,000$ K, as suggested by Verner et al. 2005 and Mehner et al. (2010).

He II was detected in the 4686 Å line that dramatically strengthens during periastron passage (Steiner & Damineli 2004; Abraham & Falceta-Gonçalves 2007; Davidson et al. 2015; Teodoro et al. 2016). At these epochs, the very fast equivalent width variability timescale (~ 1 week) indicates that the optical emission comes from a compact source, not larger than 0''.5, which coincides with the size of the He30 α image.

3.5 High velocity H30 α emission

Figures 8 and 9 present the iso-velocity raster images of the H30 α negative and positive high velocity emission, respectively, integrated over 14.6 km s $^{-1}$ velocity intervals, superimposed on the continuum contour map. The maximum flux densities between -205 and -511 km s $^{-1}$, and 28 and 247 km s $^{-1}$, are 0.43 ± 0.09 Jy beam $^{-1}$ at -350 km s $^{-1}$ and 0.13 ± 0.02 Jy beam $^{-1}$ at 115 km s $^{-1}$, respectively.

The negative high velocity emission is concentrated in a compact region, to the south-east of the continuum source and has little structure, although it resembles the 40 mas Bry and continuum images of η Car, obtained with the ESO Very Large Telescope Interferometer (VLTI) and the AMBER instrument (Weigelt et al. 2016). The positive high velocity emission arises from a weaker and more extended region, to the north-west of the compact source.

Figure 10 shows contour maps of the positive and negative flux densities, integrated over the line profile, between velocities 22 and 250 km s $^{-1}$ and -590 and -252 km s $^{-1}$, respectively, superimposed on the continuum raster image. The positive and negative high-velocity emission seem to be aligned with the Homunculus axis. This can be better seen in Figure 11, where raster images of the H30 α line peak flux density are shown for both negative and positive velocities, superimposed on the continuum contour map. Inserts with the raster images of the line peak velocity, superimposed on contour maps of the peak flux density show that for positive velocities there is a stratified velocity distribution in the north-west direction, with low positive velocities in the region of the compact continuum source, extending to 160 km s $^{-1}$ at the north end, including a narrow region in the middle, with 180–200 km s $^{-1}$ velocities. The raster images of negative peak velocities do not present any

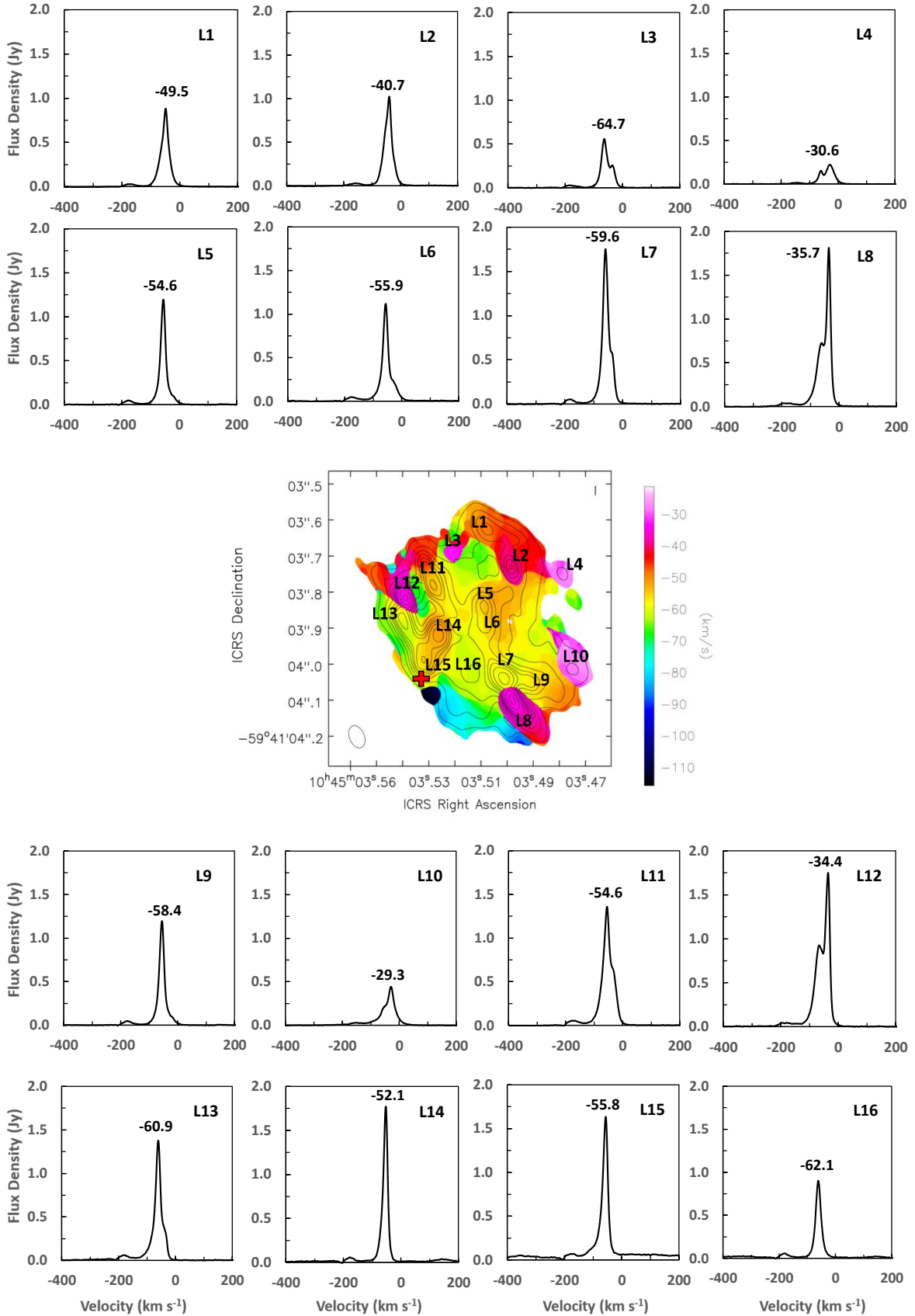


Figure 6. Individual spectra of the sixteen regions identified in the first moment image of H30 α (L1-L16), integrated over a circle of 66 mas diameter. The velocities are identified by the color scale shown on the right of the central panel. The numbers on top of the lines represent the peak velocity in km s⁻¹. The red cross in the image represents the position of the compact continuum source.

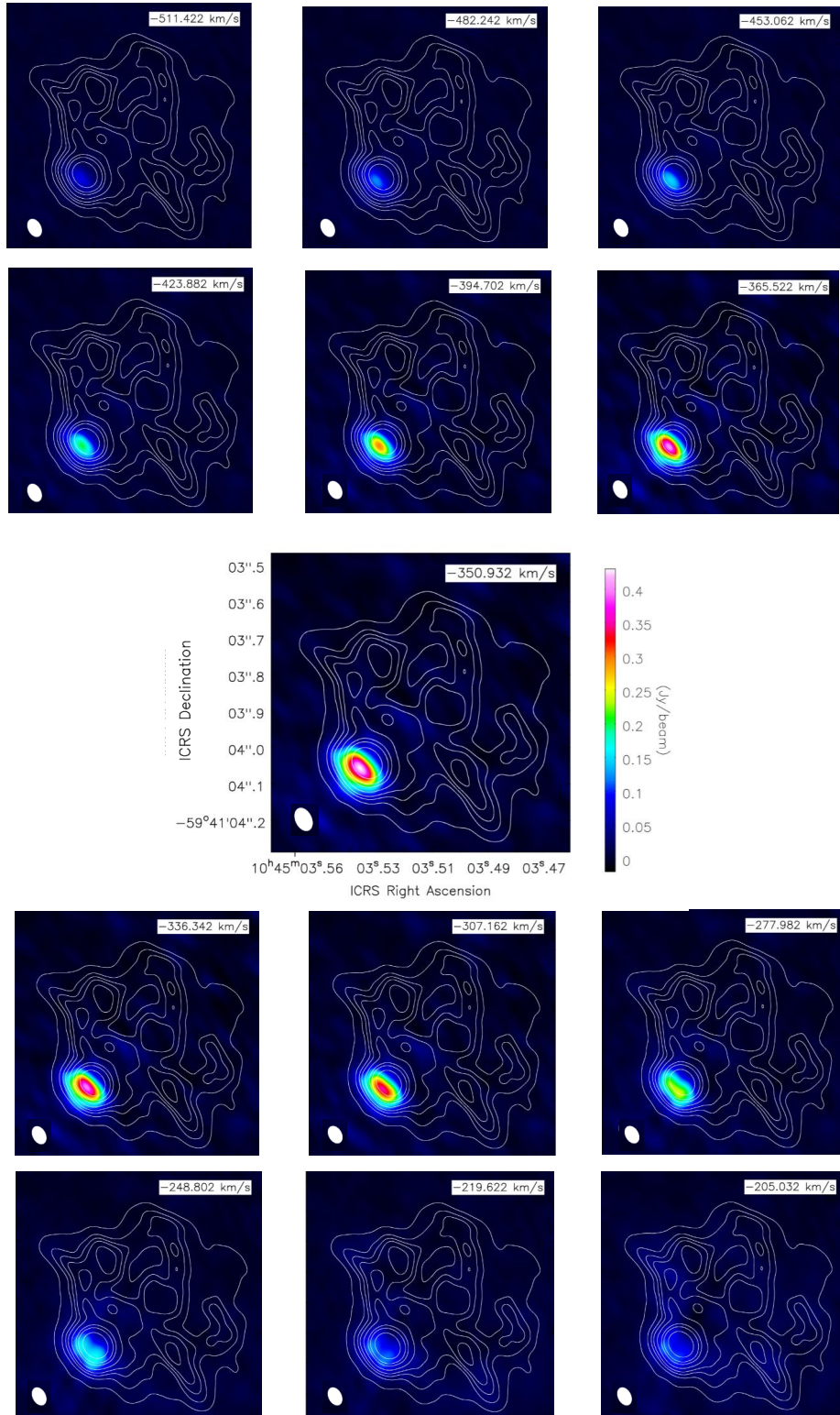


Figure 8. Velocity-integrated intensity maps of the high negative velocity H30 α emission line, integrated in bins of 14.6 km s⁻¹. All the maps have the same intensity scale (shown on the right axis of the middle panel). The center velocities are indicated in the upper right corners of each panel. The H30 α maps are superimposed on the 230 GHz continuum map shown as contours (using the same levels as in Fig. 1). The synthesized beam is shown in the bottom left corner.

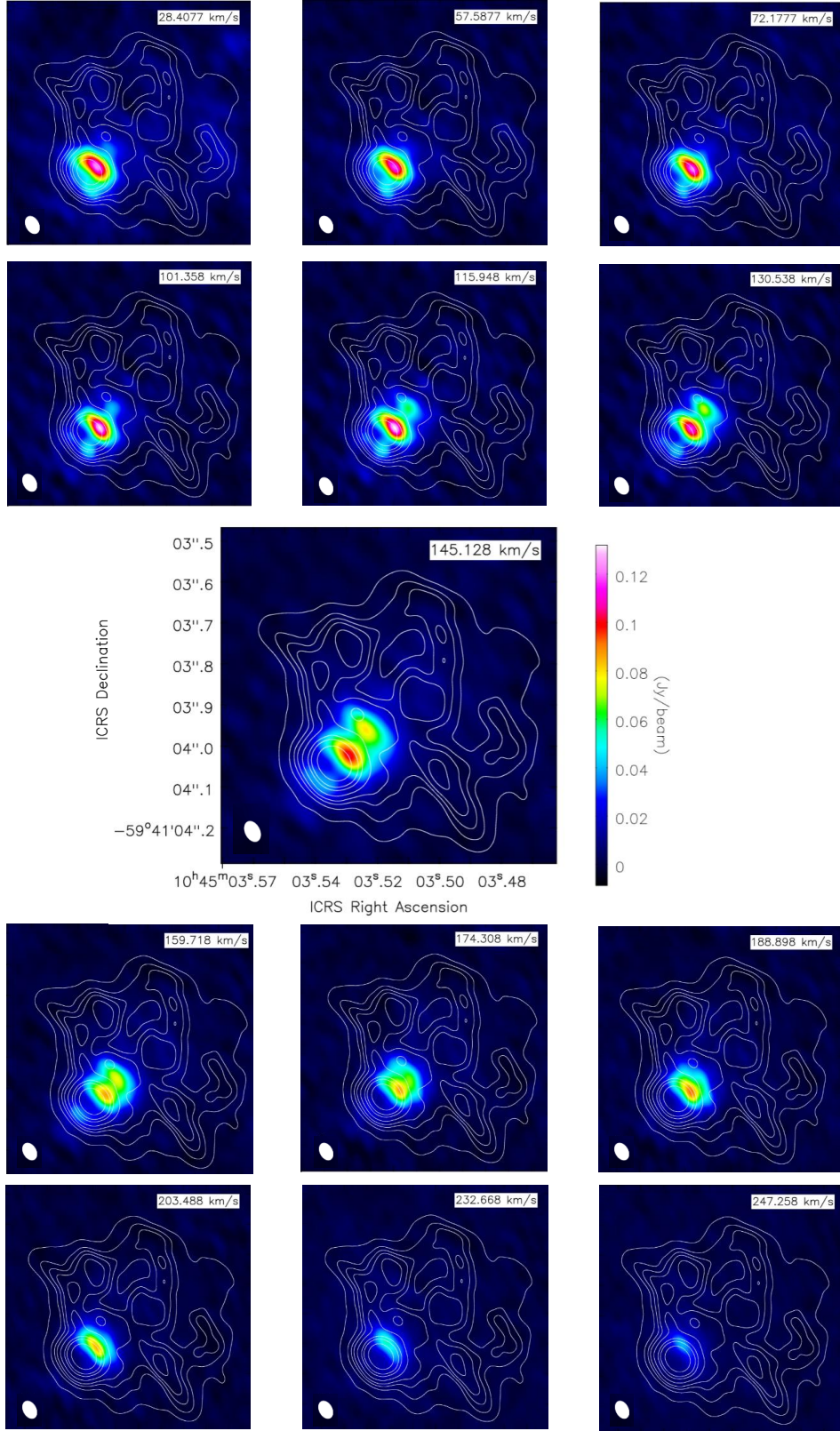


Figure 9. Velocity-integrated intensity maps of the high positive velocity H30 α emission line, integrated in bins of 14.6 km s⁻¹. All the maps have the same intensity scale (shown on the right axis of the middle panel). The center velocities are indicated in the upper right corners of each panels. The H30 α maps are superimposed on the 230 GHz continuum map shown as contours (using the same levels as in Fig. 1). The synthesized beam is shown in the bottom left corner.

Table 1. Properties of the strongest features embedded in the extended continuum and H30 α emission region of the image shown in Fig. 5

Comp.	RA ^a	Dec ^b	S(cont) ^c	S(H30 α)	V(H30 α)	HPW	S(He30 α)	V(He30 α) ^d	D ^e	PA	EM(cont)	EM(H30 α)
		"	Jy beam ⁻¹	Jy beam ⁻¹	km s ⁻¹	km s ⁻¹	Jy beam ⁻¹	km s ⁻¹	"	°	10 ¹⁰ cm ⁻⁶ pc	10 ¹⁰ cm ⁻⁶ pc
C ^f	3.532	3.980	1.13									
L1 ^g	3.508	3.626	0.23	1.23	-49.5	26	0.027	-46 [*]	0.4	332.8	7.2	12.2
L2 ^g	3.499	3.731	0.28	1.54	-40.7	27	0.027	-41	0.35	314.9	9.0	15.8
L3 ^g	3.517	3.739	0.18	0.70	-64.7	25	0.022	-47	0.27	334.8	5.0	6.6
L4	3.479	3.747	0.13	0.30	-30.6	32			0.46	300.1	3.9	3.7
L5	3.509	3.840	0.29	1.60	-54.6	20	0.052	-55	0.22	308.8	9.4	12.2
L6	3.508	3.898	0.33	1.44	-55.9	21	0.049	-56	0.20	294.3	10.9	11.5
L7	3.501	4.035	0.38	2.43	-59.6	21	0.038	-56	0.24	256.8	12.9	19.4
L8	3.498	4.097	0.38	2.76	-35.7	18	0.038	-55	0.28	245.6	12.9	18.9
L9	3.491	4.046	0.22	1.43	-58.4	20	0.052	-60	0.32	258.0	6.9	10.9
L10	3.475	4.011	0.22	0.60	-29.3	33	0.030	-30	0.43	265.9	6.9	7.5
L11	3.528	3.782	0.43	1.86	-54.6	30	0.056	-45	0.20	351.3	15.1	21.2
L12	3.539	3.813	0.40	2.70	-34.4	21	0.045	-56	0.18	17.6	13.8	21.6
L13	3.540	3.879	0.34	1.92	-60.9	21	0.061	-60	0.12	31.0	11.3	15.3
L14	3.526	3.918	0.38	2.51	-52.1	17	0.058	-60	0.08	323.8	12.9	16.2
L15	3.532	3.988	0.59	2.25	-55.8	21	0.070	-56	0.01	359.0	23.1	18.0
L16	3.516	3.941	0.29	1.06	-62.1	22	0.056	-56	0.13	287.8	9.4	8.9

^a seconds from 10^h45^m, uncertainty 0^o001

^b arc sec from -59°41', uncertainty 0^o001

^c Estimated errors: S(cont) = 0.04 Jy/beam, S(H30 α)=0.04 Jy/beam, V(H30 α)=1 km s⁻¹, HPW=2 km s⁻¹, S(He30 α)=0.04 Jy/beam, V(He30 α)=1 km s⁻¹

^d The HPW of the He30 α line is not presented because it is blended with the negative velocity H30 α line

^eDistance to the compact continuum source

^f compact continuum source

^gThe three first blobs, L1, L2, and L3 correspond to the Weigelt blobs D, C and B, respectively.

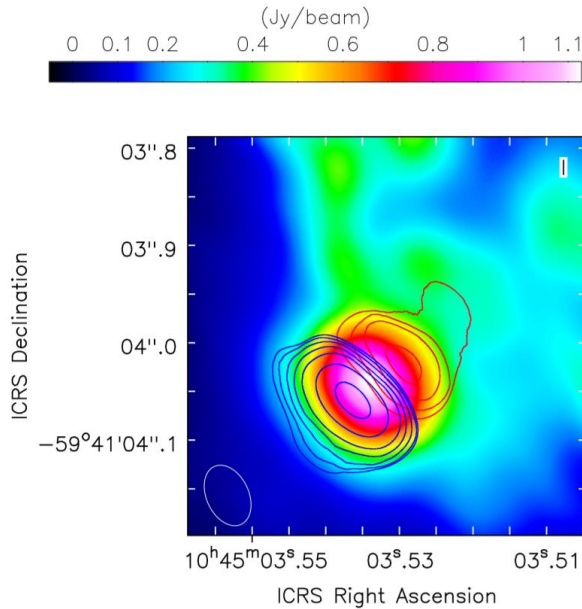


Figure 10. Contour map of the positive and negative high velocity H30 α emission, integrated over the line profile between velocities 22 and 250 km s⁻¹ and -590 and -252 km s⁻¹, respectively, superimposed on the continuum raster image. Blue contours represent negative velocities, red contours positive velocities. The contours are: : 0.05, 0.12, 0.2, 0.3, 0.4, 0.6 and 0.9 of 64.6 Jy beam⁻¹ km s⁻¹.

conspicuous structure, being concentrated between -300 and -350 km s⁻¹.

The combination of blue and red-shifted H30 α emission defines the wind emission in the direction of the Homunculus nebula, that is, perpendicular to the plane of the binary orbit, probably coincident with the rotation axis of η Car.

Similar velocity and spatial structure were observed by Mehner et al. (2010) in the [Fe III] λ 4659 line, detected with *HST*/STIS in the period 1998 to 2004; the line velocity extends from -250 to -400 km s⁻¹ at the position of η Car, reaching 0^o1 in the NE-SW direction and was attributed to the stellar wind at low latitudes. The lack of a corresponding redshifted emission was attributed to dust absorption. This structure is exactly what is observed in the H30 α recombination line except that the redshifted emission is present, although with lower intensity, probably due to absorption by the optically thick free-free source surrounding η Car, as discussed in Section 4.2

3.6 The H bar

As mention in Section 3.2, the compact source line profile shows a weak -100 km s⁻¹ component, blended with the stronger line centered at -58 km s⁻¹. The iso-velocity images presented in Figure 12 confirm the existence of a single source of emission, to the southwest of the compact continuum source, with velocities extending from -130 km s⁻¹ to lower negative velocities, reaching a maximum flux density of 0.6 Jy beam⁻¹ at -86 km s⁻¹, velocity at which it starts to blend with other components of the extended north-west region. The -100 km s⁻¹ component can be followed up to lower velocities in Figure 4, in a different flux density scale, until it disappears at -72 km s⁻¹.

This structure can be associated with the 1" length H α bar de-

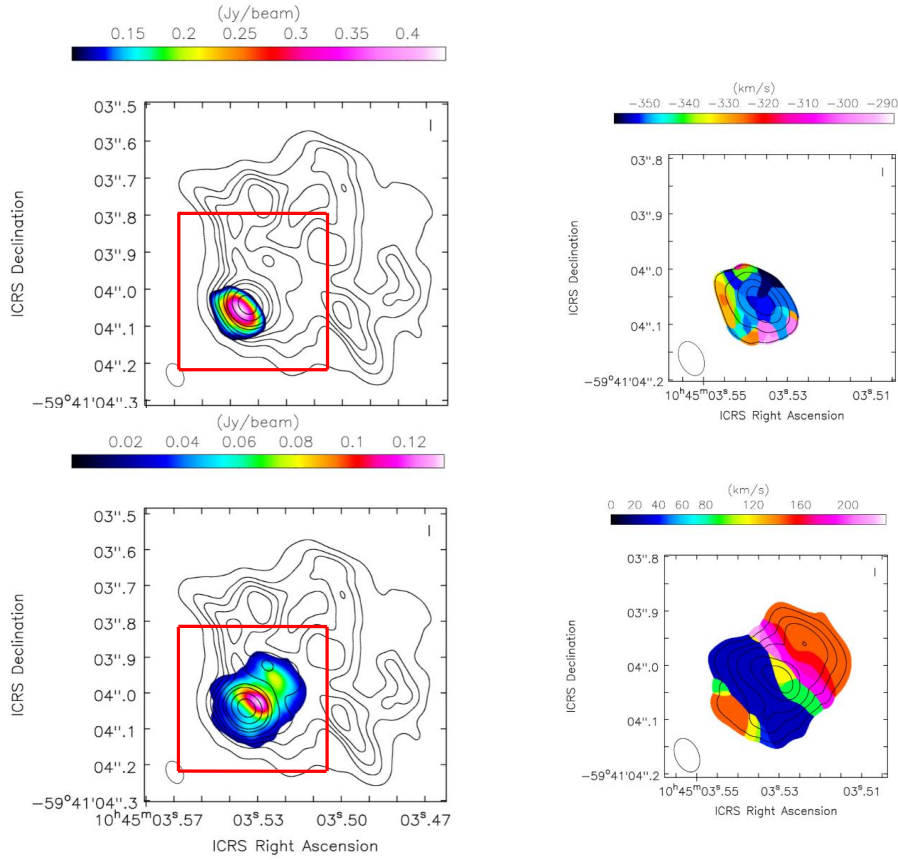


Figure 11. Top left: raster image of the high negative velocity line emission zero momentum, integrated between -286 and -357 km s^{-1} , superimposed to the continuum contour map. Bottom left: the same as top left, but for high positive velocities integrated between 28 and 232 km s^{-1} . Continuum map contour levels are the same as in Figure 1. Red squares represent the inserts shown to the figure right. Top right: contour map of the negative high velocity zero momentum, superimposed to the velocity weighted (first momentum) raster image. Contours are $0.25, 0.4, 0.6$ and 0.8 of 0.435 $\text{Jy beam}^{-1} \text{ km s}^{-1}$. Bottom right: the same as top right for high positive velocities. Contours are: $0.2, 0.3, 0.4, 0.6$ and 0.8 of 0.132 $\text{Jy beam}^{-1} \text{ km s}^{-1}$

ected by Falke et al. (1996) using speckle imaging polarimetry. The sharp intensity drop found in the polarized optical line in the NW to SE direction was interpreted as absorption by a dusty equatorial disk around η Car, with its rotation axis along the major Homunculus axis (Falke et al. 1996). However, since the $\text{H}30\alpha$ line is not affected by absorption, the asymmetry in the bar seems to be real.

4 DISCUSSION

The high angular resolution of the new ALMA data enabled to detect extended emission to the north-west of η Car in the continuum and the $\text{H}30\alpha$ emission line, revealing a large number of compact, unresolved components with different velocities (Figs. 1, 4 and 6).

A strong unresolved continuum source is observed at the position of the binary system and high velocity $\text{H}30\alpha$ emission is detected in its spectrum in the direction of the Homunculus axis, probably associated with the aspherical wind of η Car.

Figure 13 shows a schematic outlining the features detected in our images. In the next Sections we discuss the nature of the emission and the physical conditions of the different regions, as well as their implications on the different models discussed in the literature.

4.1 The Central Source

The detection of high energy emission by Fermi/LAT and H.E.S.S., and its variability along the orbital period of η Car (Reitberger et al. 2015; Hamaguchi et al. 2018; Abdala et al. 2020) rise the question of how much of the continuum radio emission is due to non-thermal synchrotron radiation.

To investigate this question, we calculate the thermal contribution of the ionized plasma, represented by the $\text{H}30\alpha$ line emission, to the total continuum emission.

First, the spectrum of the $\text{H}30\alpha$ line, integrated over a circle of 90 mas radius centered on η Car, was fitted by five Gaussian components that represent the negative and positive high velocity winds (G1 and G5), the $\text{He}30\alpha$ line (G2), the H bar (G3), and the narrow line, possibly resulting from the superposition of the NW source (G4).

Table 2 presents the peak flux density, the central velocity and line width of each Gaussian component and Figure 14 shows the observed spectrum, the fitted Gaussians and the residuals of the fitting.

The emission measure EM_L of each component, calculated from its line, is also presented in Table 2; it was obtained assuming a plasma with electron temperature T_e of 10^4 K, optically thin to the $\text{H}30\alpha$ line radiation, which has a maximum brightness temperature

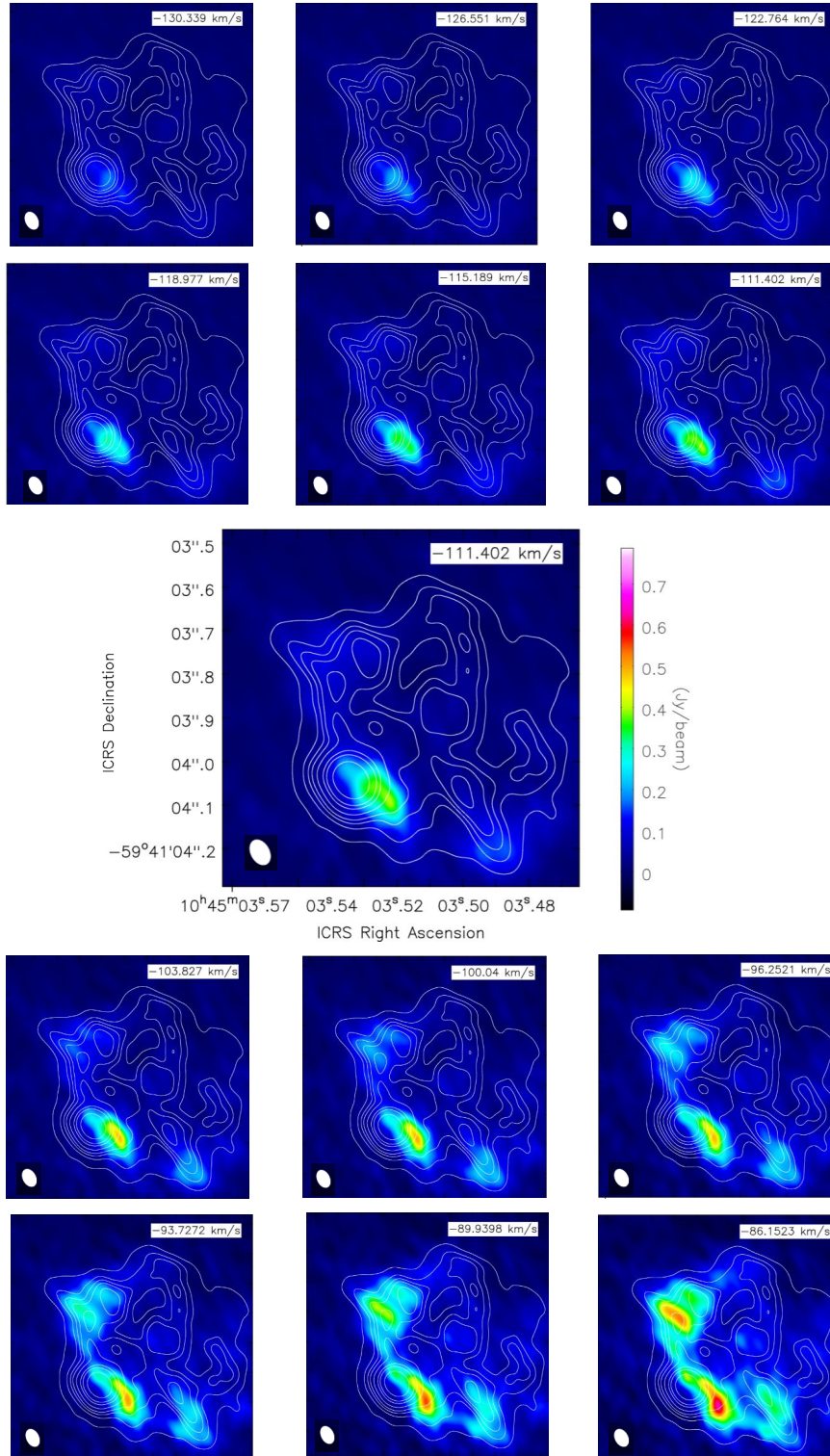


Figure 12. Velocity-integrated intensity maps of the -100 km s^{-1} component of the $\text{H}30\alpha$ emission line, integrated in bins of 1.262 km s^{-1} . All the maps have the same intensity scale (shown on the right axis of the middle panel). The center velocities are indicated in the upper right corners of each panels. The $\text{H}30\alpha$ maps are superimposed on the 230 GHz continuum map shown as contours (using the same levels as in Fig. 1). The synthesized beam is shown at the bottom left corner.

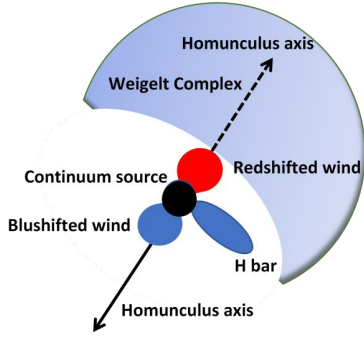


Figure 13. Schematic showing the different features detected in the continuum and H30 α images of η Car

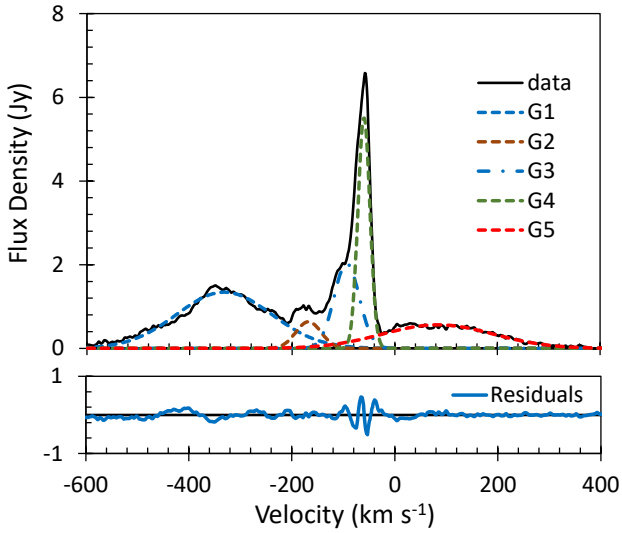


Figure 14. H30 α spectrum of the central source (integrated over a 90 mas radius region) and the five individual Gaussian components fitting the line (see text).

T_L :

$$T_L = 1.92 \times 10^3 \left(\frac{T_e}{K} \right)^{-1.5} \left(\frac{EM_L}{\text{cm}^{-6}\text{pc}} \right) \left(\frac{\Delta\nu}{\text{kHz}} \right), \quad (1)$$

where $\Delta\nu$ is the line width in kHz. The brightness temperature T_L is related to the measured flux density S_L by:

$$S_L = \frac{2kT_L\nu_L^2}{c^2} \Omega, \quad (2)$$

where ν_L is the central frequency of the line, Ω the solid angle of the source and c the speed of light. The solid angle is calculated from:

$$\Omega = \pi \frac{\theta_{\text{maj}}\theta_{\text{min}}}{4 \ln 2}, \quad (3)$$

where θ_{maj} and θ_{min} are twice the major and minor axis of the ellipse that represent the source (in our case both equal to 180 mas).

The emission measure necessary to explain the continuum

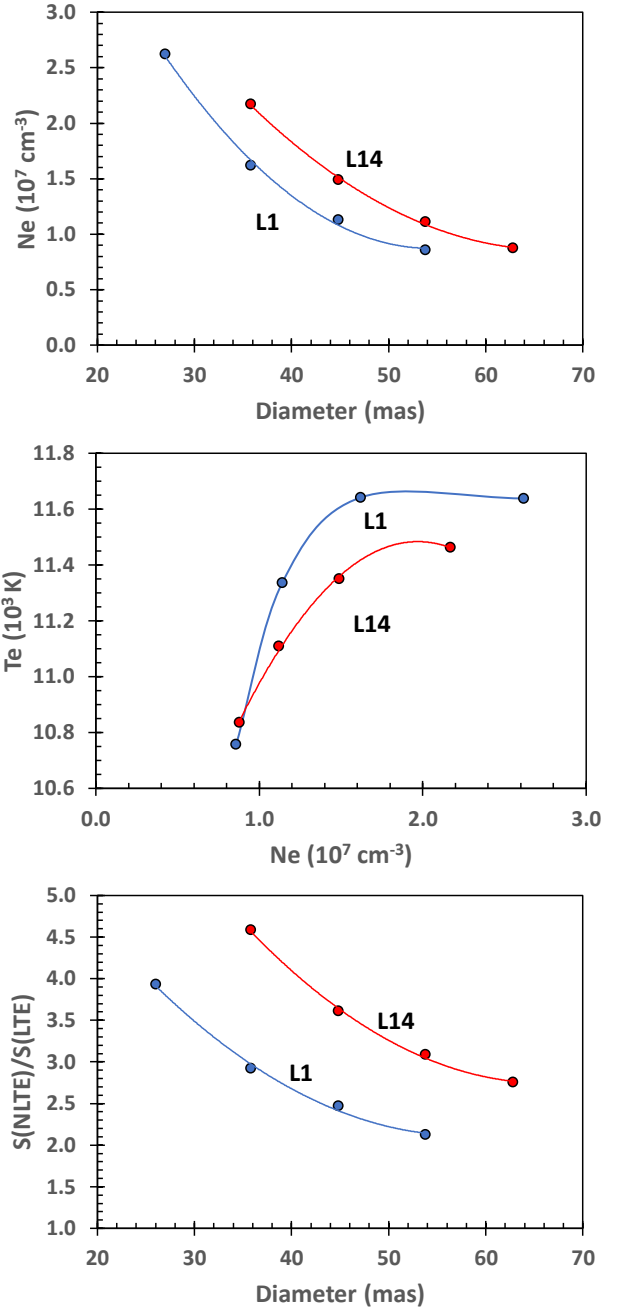


Figure 15. Physical parameters of homogeneous spheres that fit the continuum flux density and maximum in the H30 α line profile of blobs L1 and L14. Top: electron density N_e vs. source diameter; middle: electron temperature T_e vs. electron density N_e ; bottom: ratio of NLTE to LTE maximum flux density

emission, EM_c assumed to be of free-free origin, is obtained from the opacity τ :

$$\tau = 3.014 \times 10^{-2} \left(\frac{T_e}{K} \right)^{-1.5} \left(\frac{\nu}{\text{GHz}} \right)^{-2} \left(\frac{EM_c}{\text{cm}^{-6}\text{pc}} \right) \langle g_{ff} \rangle \quad (4)$$

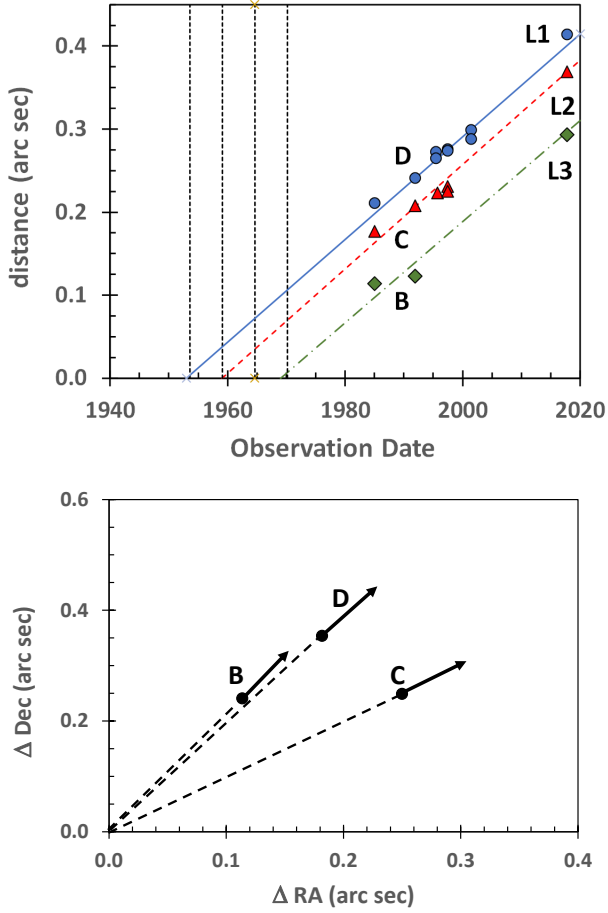


Figure 16. Top: distance to the core of Weigelt blobs B, C, and D (L3, L2 and L1, respectively) as a function of time. Vertical lines correspond to epochs of minimum intensity in the high ionization lines. Bottom: position of the Weigelt blobs relative to the continuum compact source; arrows represent velocities

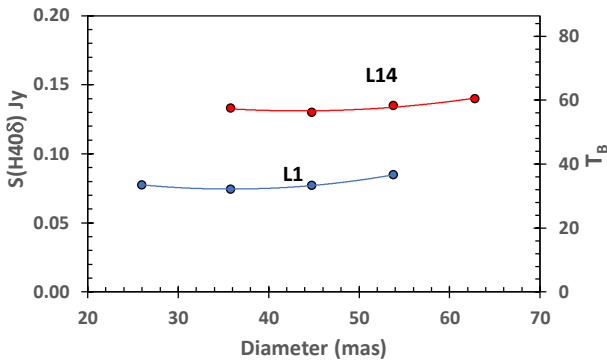


Figure 17. Intensity of the H40 δ line for the compact sources L1 and L14, for the same models than those in Figure 15

Table 2. Parameter of the five Gaussian components fitting the H30 α emission line.

Name	V_L km s $^{-1}$	S_L Jy	Δv km s $^{-1}$	EM 10^{11} cm $^{-6}$ pc
G1	-332.5	1.34	217.6	1.02
G2	-168.3	0.64	58.1	0.41
G3	-93.8	2.03	57.8	0.53
G4	-60.1	5.51	27.6	0.50
G5	83.9	0.56	254.0	0.13

with

$$\langle g_{ff} \rangle = \ln \left[4.955 \times 10^{-2} \left(\frac{v}{\text{GHz}} \right)^{-1} \right] + 1.5 \times \ln \left(\frac{T_e}{\text{K}} \right) \quad (5)$$

The opacity τ is obtained from the observed flux density S_c :

$$S_c = \frac{2kT_e v^2}{c^2} (1 - e^{-\tau}) \Omega. \quad (6)$$

From Table 2 we find that the total emission measure necessary to account for the line intensity is 2.59×10^{11} cm $^{-6}$ pc, while that necessary to explain the continuum is 2.46×10^{11} cm $^{-6}$ pc, showing that all the continuum emission can be explained by thermal processes, at least during the orbital phases in which the stars are farther apart. During the 2003.5 periastron passage, Abraham et al. (2005) found, in single dish daily observations, a 1 Jy increase in the 7 mm continuum lasting for a week, which they attributed to emission from the shocked region formed by the colliding winds. More high resolution data at different orbital phases of the binary system are needed to confirm this assumption.

4.2 The high velocity winds

The contribution of the η Car wind to the total continuum emission can be obtained by dividing the emission measure calculated from its spectral lines G1 and G5, presented in Table 2, by the emission measure derived from the total spectrum.

Even if we exclude the strong narrow line, the remaining H30 α line profile of the compact source differs from the 0.15 resolution H δ profiles obtained by Nielsen et al. (2007) with the *Hubble Space Telescope* Space Telescope Imaging Spectrograph (*HST/STIS*) during a complete binary cycle, which show smooth lines centered at approximately the systemic velocity of η Car and extending to ± 500 km s $^{-1}$. As the continuum spectrum reported in Paper I presents characteristics of a compact H II region that becomes optically thin ($\tau \sim 1$) around 300 GHz, the asymmetry in the high velocity H30 α spectrum can be attributed to absorption, if part of the material that produces the positive velocity line is behind the continuum source. Therefore, we consider that the total wind emission is twice the value of the blueshifted component flux density and compare it to the theoretical value expected from free-free emission of an ionized wind (Panagia & Felli 1975):

$$S_{\nu}(\text{wind}) = 5.12 \left[\frac{v}{10 \text{ GHz}} \right]^{0.6} \left[\frac{T_e}{10^4 \text{ K}} \right]^{0.1} \left[\frac{\dot{M}}{10^{-5} M_{\odot} \text{ yr}^{-1}} \right]^{4/3} \times \left[\frac{v_{\infty}}{10^3 \text{ km s}^{-1}} \right]^{-4/3} \left[\frac{d}{\text{kpc}} \right]^{-2} \quad (7)$$

Using $10^{-3} M_{\odot} \text{ yr}^{-1}$ for the mass loss rate \dot{M} and 500 km s $^{-1}$ for the

terminal wind velocity v_∞ we obtain $S_\nu(\text{wind}) = 7.4$ Jy. The value derived from the observations is 3.7 Jy, smaller than the theoretical value. The reason is that because of the fast rotation of η Car, its wind is aspherical and the mass loss rate and velocity depend on latitude θ (Dwarkadas & Owocki 2002) as:

$$\dot{M}(\theta) = \dot{M}(90^\circ) \left[1 - \omega^2 \cos^2(\theta) \right] \quad (8)$$

$$v_\infty(\theta) = v_\infty(90^\circ) \left[1 - \omega^2 \cos^2(\theta) \right]^{1/2}, \quad (9)$$

ω is the rotation velocity of η Car relative to the critical value of $(GM/R^3)^{1/2}$, where G is the gravitational constant and M and R its mass and radius.

Taking into account that the wind is not isotropic, the observed terminal velocity is the projection of the real terminal velocity into the line of sight. Assuming that the rotation axis of η Car coincides with the Homunculus axis, the true terminal velocity is ~ 700 km s^{-1} , compatible with the values measured by Smith et al. (2003a). The effect of including the latitude dependence of the mass loss rate and wind velocity assuming $\omega = 0.9$ is to decrease the expected flux density by 67%, while the increase in the terminal velocity will decrease it by 63%, resulting in an expected flux density from the wind of 3.2 Jy, in agreement with the 3.7 Jy derived from the observations.

The radius R_v at which half of the wind continuum radiation is emitted was also derived by Panagia & Felli (1975):

$$R_v(\text{wind}) = 6.23 \times 10^{14} \left[\frac{\nu}{10 \text{ GHz}} \right]^{-0.7} \left[\frac{T_e}{10^4 \text{ K}} \right]^{-0.45} \times \left[\frac{\dot{M}}{10^{-5} M_\odot \text{ yr}^{-1}} \right]^{2/3} \left[\frac{v_\infty}{10^3 \text{ kms}^{-1}} \right]^{-2/3} \text{ cm} \quad (10)$$

Using this expression we find the extension of the wind in the directions of the Homunculus axis is ~ 130 AU or ~ 60 mas, in agreement with the observations presented in Figure 10.

The critical value of the mass loss rate that can be fully ionized by η Car was calculated by Morse et al. (1998) as $3.3 \times 10^{-4} M_\odot \text{ yr}^{-1}$; since the value inferred from the spectra is smaller than that attributed to η Car, the ionizing front must be trapped inside the wind. Although it is possible that the dense base of the wind is ionized by collisions or by Balmer continuum photons, as discussed by Natta & Giovanardi (1991), it is still necessary to add the ionizing photons of the companion star to account for the ionization of the extended NW region. This raises the question of the position of the companion star relative to η Car during the ALMA observations. Although the observations were obtained close to apastron, single dish observations during the complete orbital period show free-free emission during all the cycle, except for a few month during periastron passage, implying that the ionizing photons reach the region during all this time. The same behavior was observed at lower frequencies and larger distances by Duncan & White (2003), meaning that the ionizing front reaches also the little Homunculus and maybe the surrounding torus or disk. For these reasons we believe that the relative position of the stars along the orbit cannot be fully derived from the ALMA data, but can be better determined by the observed and modeled position of the fossil material left by the wind-wind collision zones.

4.3 The physical parameters of the NW compact regions

The spectrum of the NW extended region is dominated by the very strong and narrow H30 α recombination line. Previous non-resolved ALMA observations (Paper I) of the recombination lines H42 α , H40 α , H30 α , H28 α , and H21 α , and their respective continuum were modeled as a homogeneous expanding ionized shell of about 0''.2 radius and 0''.02 width, with an electron density $n_e = 1.3 \times 10^7 \text{ cm}^{-3}$ and a temperature $T_e = 1.7 \times 10^4$ K.

The size of the shell agrees with the present observations and its width is smaller than the HPBW, but the velocity distribution shown in Figure 6 is not compatible with that of an expanding shell; instead the velocities of the different compact components seem to follow a random pattern.

In Table 1 we present the EM s of the compact components inferred from the line profiles assuming LTE conditions and their sizes equal to the beam size, and also the EM s inferred from the underlying free-free continuum; equations 1-6 were used in the calculations. In most of the sources, the EM derived from the lines is larger than that derived from the continuum, a clear sign of NLTE.

To investigate the physical conditions of the observed individual non resolved sources, we assume that they are homogeneous ionized spheres, with diameter D smaller than the HPBW. We solved the NLTE transfer equations as in Paper I and determined the combination of T_e , n_e and D values necessary to match simultaneously the observed continuum flux density and maximum line intensity, as presented in Table 1. We modeled two components, L1 and L14, because each one of them seems to arise from a single velocity region. We first selected a value for the diameter and three values for T_e : (1.0, 1.1 and 1.2) $\times 10^4$ K, and determined the values of n_e necessary to match the observed continuum flux density, obtaining the values of the line maximum flux density. We then obtained, by interpolation, the values of T_e and n_e for which the model and observed line flux density coincide. We repeated the procedure for different values of the source diameter; the results are presented in Figure 15, with the combinations of n_e vs. D in the top panel, T_e vs. n_e in the middle and the line amplification, represented by the ratio of the NLTE to LTE maximum line intensity in the bottom. The values of n_e are compatible with what was found in Paper I although T_e is somehow smaller, more compatible with the temperature expected in a compact H II region.

For both sources and for all the physical conditions presented in Figure 15, the turnover frequency of the continuum spectrum (where $\tau \sim 1$) is very close to the frequency of observation. This is consistent with the spectrum between 90 and 670 GHz measured with ALMA during Cycle 0 (Paper I).

The mass of the model sources vary between 0.9 and $3.0 \times 10^{-5} M_\odot$ for L1 and 1.8 and $4.0 \times 10^{-5} M_\odot$ for L14, for increasing values of D . Considering that all the compact sources have similar masses, we obtain a total mass for the extended region of $10^{-4} - 10^{-3} M_\odot$. A similar result was obtained using the mean density of the extended region necessary to reproduce the observed continuum flux density ($n_e = 2.8 \times 10^6 \text{ cm}^{-3}$ for $D = 1.8 \times 10^{16} \text{ cm}$).

4.4 Comparison with observations at other wavelengths

The detection of a large number of compact (< 60 mas) sources within 0''.6 to the north-west of η Car, emitting in the 230 GHz continuum and in the H30 α and He30 α recombination lines, with densities and temperatures of the order of 10^7 cm^{-3} and 10^4 K, as estimated in the previous subsection, must be analyzed in the

context of previous observations of the same region at different wavelengths and with similar resolutions.

The region, labeled by [Chesneau et al. \(2005\)](#) the "Weigelt Complex", was intensively studied since the discovery, using speckle interferometry techniques, of compact sources (< 30 mas) at distances smaller than $0''.3$ from η Car ([Weigelt et al. 1995](#); [Hofmann & Weigelt 1988](#)). The brightest sources besides source A, identified with the star, were labeled "Weigelt blobs" B, C, and D; they present narrow permitted lines of H, He and Fe II, and forbidden lines of [N I], [Fe II], [Ne III], [Fe III], and other ions, with heliocentric velocities in the range of -45 to -48 km s $^{-1}$ and FWHM of about 22 km s $^{-1}$ ([Davidson et al. 1995, 1997](#)). The UV to IR spectra of the Weigelt blobs is also affected by resonance fluorescence, occurring specially in the Fe II lines, but also in O I, Cr II, Fe III, and Ni II. In these ions, the upper energy levels are overpopulated because of energy coincidence with H I Ly α photons ([Johansson et al. 2000](#); [Johansson & Letokhov 2001](#); [Johansson et al. 2005](#)). The existence of these transitions imply that the Ly α photons must be local.

The physical conditions of the regions that present spectra of low ionization elements was estimated from emission models as $n_e \sim 10^6$ cm $^{-3}$ and $T_e \sim 7000$ K ([Verner et al. 2002](#)). Models of spectra of high ionization elements and high excitation lines, on the other hand, require photoionized regions of H $^+$ and He $^+$ with densities and temperatures of 10^7 cm $^{-3}$ and 10^4 K ([Verner et al. 2005](#); [Mehner et al. 2010](#)). The narrow line spectra of the high ionization elements show also strong dependence on the phase of the binary orbit, disappearing completely during the spectroscopic events, while the lines of the low ionization elements, like those of [Fe II] remain visible, and are even enhanced ([Johansson et al. 2000](#); [Smith et al. 2004](#); [Hartman et al. 2005](#); [Nielsen et al. 2007](#); [Mehner et al. 2010](#); [Hamann 2012](#); [Remmen, Davidson & Mehner 2013](#); [Gull et al. 2016](#)).

The nature of the Weigelt blobs was explained by different models, which were modified as new observational evidences became available. The first models assumed that the blobs are formed by neutral H, extending from the ionizing O type supergiant or WR star to distances of $0''.3$ or more; as a consequence, the high ionization elements are found in an extended region close to the ionizing source while the low ionization material populates a narrow region at the surface of the blobs ([Verner et al. 2002](#); [Johansson & Letokhov 2001](#)). This model was contested by [Remmer et al. 2013](#), because the ions with higher ionization energy were observed at larger distances from the star. A new qualitative model, similar to that proposed by [Smith et al. \(2004\)](#), assumed that the blobs are dense condensations of low ionization material, with its surface ablated by photoionization, and that the evaporated material, now highly ionized, moves outward around the condensation, accelerated by radiative forces.

Another constrain for the models came from the infrared observations obtained with the ESO/VLT Adaptive Optics system NACO and narrow band filters centered at the wavelengths of the H P γ and Br α lines, which showed Weigelt blobs C and D clearly resolved. These observations were interpreted as evidence of the existence of dust inside the blobs ([Chesneau et al. 2005](#)). However, comparison of the 3.74 μ m (P γ) image with red continuum images of the blobs presented by [Morse et al. \(1998\)](#) did not show perfect spatial coincidence at both wavelengths, which raised the possibility that the blobs are part of a larger region that become visible only where the dust absorption is lower. In fact, dust grains can condensate at the location of the Weigelt blobs ([Falke et al. 1996](#)). [Davidson et al. \(1997\)](#) estimated the grain temperature at this site to

be ~ 1000 K. However, the presence of the 10^4 K source detected by ALMA will probably destroy the grains, if present.

The ALMA observations reported in this paper show the existence of compact fully ionized regions, with densities and temperatures similar to those necessary to explain the spectra of low and high ionization elements in the Weigelt Complex, as well as the high excitation lines. Their radial velocities are also similar to those of the UV-IR lines, considering that the former are relative to the LSR while the latter are heliocentric, and there is a difference of -11.6 km s $^{-1}$ between them. All these considerations suggest the identification of the compact radio sources with the UV to IR blobs in the Weigelt Complex.

It should be pointed out that it is the high velocity resolution of the ALMA observations that allowed the identification of compact sources, otherwise, they would appear as larger condensations of matter with a wider velocity profile, as observed by [Remmer et al. 2013](#). In a similar way, the UV to IR spectra of the blobs show that the lines of different elements originate in different positions and can have different velocities ([Smith 2004](#)), and therefore are probably formed in different compact radio sources.

There is still a question that remains to be treated: the existence of dust in the center of the Weigelt blobs, as suggested by the IR observations of [Chesneau et al. \(2005\)](#). Analysis of these observations show that the Weigelt blobs were only conspicuous in the narrow filters with central wavelengths coincident with the hydrogen lines P γ and Br α ; the P γ line was calibrated, resulting in a flux density of 520 ± 70 Jy for the central source, identified as η Car, and lower flux densities for the other detected blobs. Based on the ALMA observations, we claim that the observed emission comes from the P γ H line instead of dust. To support this assumption we calculated the expected P γ line flux density $S(\text{P}\gamma)$ of one of our typical compact sources, by scaling the emissivity coefficients ϵ of the H30 α and P γ transitions, for ionized H density of 10^7 cm $^{-3}$ and temperature 10^4 K given by [Storey & Hummer \(1995\)](#). The resulting flux density of the P γ line is given by:

$$S(\text{P}\gamma) = \frac{\epsilon(\text{P}\gamma)}{\epsilon(\text{H}30\alpha)} \frac{\nu(\text{H}30\alpha)}{\nu(\text{P}\gamma)} S(\text{H}30\alpha) \quad (11)$$

The ratio of the emissivity coefficients is 8.7×10^3 , and the flux density of the H30 α line is $S(\text{H}30\alpha) \sim 2$ Jy, for a source of 50 mas diameter, resulting in an expected flux density of 47 Jy for the P γ emission of the compact radio source. Considering that there can be a superposition of sources in the 100 mas beam of the IR observation, we find $S(\text{P}\gamma) = 190$ Jy for the IR blob, showing that the observed IR emission can be explained by H line emission, and that the presence of dust emission is not required.

A complementary argument is obtained from the excellent agreement between the structures seen in the 230 GHz continuum and in the Br α images in Figure 2. Since the images obtained with wider filters, which are dominated by dust emission, do not show these structures, we conclude that the dust is located between the compact regions and the observer, shielded from the UV radiation necessary to sustain the ionized plasma detected in the ALMA observations. The existence of this gas layer is corroborated by the absorption of CO and HCN in front of the continuum source detected by [Bordiu & Rizzo \(2019\)](#) at 345 GHz.

4.5 The Weigelt blobs

In the previous subsection we identified the compact radio sources with the UV-IR blobs seen in the Weigelt Complex.

The origin and evolution of these blobs is not clear; [Davidson](#)

et al. (1997), Smith et al. (2004) and Dorland et al. 2004, studied the proper motions of Weigelt blobs C and D, and attributed them to ejections that occurred some time between 1910 and 1941.

In order to determine more accurately the ejection epochs of the blobs and their proper motions, we used their measured positions at previous epochs to estimate their probable position at the epoch of our observations. We were able to identify blobs C and D with the compact sources L2 and L1, with position angles 315° and 333° , respectively. We tentatively identified Weigelt blob B with L3, although it was only present in the Weigelt & Ebersberger (1986) observations. Their positions relative to η Car are shown in Figure 16. The velocities, obtained from a linear fitting of their positions are $6.2 \pm 1.6 \text{ mas yr}^{-1}$, $6.0 \pm 1.6 \text{ mas yr}^{-1}$ and $5.7 \pm 2.3 \text{ mas yr}^{-1}$, for blobs D (L1), C (L2) and B (L3), respectively. The linear velocity corresponding to an angular velocity of 6 mas yr^{-1} is 67 km s^{-1} , similar to the Weigelt blobs radial velocities. The ejection epochs obtained from the linear fitting are 1952.6, 1957.1 and 1967.6, respectively. In the upper part of Figure 16 we also show the epochs of minimum in the high excitation line intensities, presumably related to periastron passage: 1953.6, 1959.1, 1964.6 and 1970.2, corresponding to cycles 2, 3, 4 and 5 according to Damineli et al. (2008), considering that the first spectroscopic event was reported by Gaviola (1953). In the lower part of the Fig. 16 we show the position of the Weigelt blobs relative to the central continuum source, with vectors indicating the direction and the relative magnitude of their velocities in the plane of the sky. We conclude that the Weigelt blobs were ejected close to periastron passage during the firsts spectroscopic events. It is possible that the other compact sources observed in the H30 α line image, closer to η Car, were ejected later, and if so, their evolution should be measured in future observations.

From the radial velocities and proper motions, we calculate the angles of the D, C and B blob's trajectories relative to the plane of the sky as $35^\circ 0'_{-6}^{+10}$, $31^\circ 2'_{-6}^{+9}$ and $45^\circ 5'_{-9}^{+14}$, all of them compatible with the position of the equatorial plane of the Homunculus nebula.

The observed angular velocities are larger than those derived previously by other authors (Davidson et al. 1997; Smith 2004; Dorland et al. 2004); the reason is the larger time span in our observations. Of course, this result depends on the accuracy of the identification of the Weigelt blobs with the compact sources detected by ALMA, but unless the blobs had already vanished, the only sources in the data with position angles and distances compatible with those of the blobs are L1, L2 and L3.

4.6 HCO+ or H40 δ emission line?

Bordiu & Rizzo (2019) reported ALMA observations of CO, HCN and HCO⁺ in the direction of η Car. The molecular gas, as traced by the CO(3-2) and HCN(4-3) emission lines, is seen in a disrupted 2" torus surrounding the binary system (see also Smith et al. 2018). In contrast, the HCO⁺(4-3) emission line is also detected in an asymmetric, extended structure north-west of the star, that coincides precisely with that of the 230 GHz continuum and H30 α line emission described in this paper. This spatial coincidence and the fact that the presence of HCO⁺ is unexpected in a highly ionized gas led us to explore further the nature of this emission line and see if it could be instead a hydrogen recombination line.

The rest frequency of the HCO⁺(4-3) line is 356.734 GHz; the nearest hydrogen recombination line is H40 δ , with a rest frequency of 356.658 GHz. Considering the difference in frequencies, if the line observed by Bordiu & Rizzo (2019) were H40 δ , the cor-

responding velocity would be -63.7 km s^{-1} , coincident with the velocity of the extended region. This coincidence strongly suggests that the 356.7 GHz emission line, outside the 2" torus is the H40 δ recombination line.

To support this suggestion, we calculated the intensity of the H40 δ line in the compact sources L1 and L14, as it was done for the H30 α line. The resulting flux densities are presented in Figure 17 as a function of the source diameter, for the same combination of electron densities and temperatures necessary to fit the 230 GHz continuum and H30 α lines. The brightness temperatures are also presented in the figure, showing that the profile of the line detected by Bordiu & Rizzo (2019) can be explained by the superposition of the line profiles of the compact sources with different velocities as detected in the H30 α line.

Although the calculations were made assuming NLTE, the line intensities show that the population is in LTE. We can notice the similarity of the -54.6 km s^{-1} image in our Figure 4 with that of Figure 4 of Bordiu & Rizzo (2019). The only difference is the intensity of components L14 and L15, which are much stronger in the H30 α line. This is consistent with the fact that those lines are amplified by NLTE effects in the H30 α lines.

Based on the spatial coincidence of the emissions of the H30 α and the 356.7 GHz emission line reported by Bordiu & Rizzo (2019) and the results of the above analysis, we conclude that the emission line centered at the position of the binary system is the H40 δ recombination line.

5 CONCLUSIONS

In this paper, we report on new ALMA high-angular resolution observations of the H30 α and He30 α recombination lines and the underlying continuum of the $0''.8 \times 0''.8$ central region of η Car. The unprecedented angular resolution of 50 mas (or 110 AU) allowed us to explore the extended emission north-west of the binary star tracing the most recent mass-loss history. The main findings based on these new observations are as follows.

1. The 230 GHz continuum, H30 α and He30 α recombination line images of η Car were resolved with the $0''.065 \times 0''.043$ beam obtained using ALMA in the extended configuration. The continuum image consists of a structureless core of $0''.12$ HPW and weaker emission extending over $\sim 0''.6$ in the NW direction that presents several regions of enhanced emission.

2. The spatially integrated spectrum is similar to that obtained in Paper I, with a strong H30 α narrow line centered at -58 km s^{-1} and much weaker extended emission at higher negative and positive velocities. The narrow line is much weaker in the spectrum integrated over the compact continuum source. The He30 α line is also detected in both spectra.

3. The high quality ALMA data allowed us to extract images of the H30 α line emission with 1.262 km s^{-1} velocity resolution, revealing that maximum emission in different regions occurs at different velocities. Sixteen compact sources with well defined velocities were identified; their spectra, when not blended, have HPW of $\sim 20 \text{ km s}^{-1}$, compatible with the thermal velocity of 10^4 K plasma. Three of these sources (L3, L2, and L1) were identified with Weigelt blobs B, C, and D, respectively.

4. The H30 α recombination line profiles of the non-resolved sources and their underlying continuum flux densities were reproduced assuming homogeneous spheres of ionized gas in NLTE, with densities and temperatures characteristic of compact H II regions (10^7 cm^{-3} and 10^4 K , respectively). These compact sources

probably represent the UV to IR blobs observed in the Weigelt Complex.

5. The high negative velocity line emission arises from a compact source SE of η Car, while the positive velocity emission extends in the NW direction. Both seem to be aligned with the Homunculus axis and to arise from the stellar wind enhanced in the polar axis of the fast rotating η Car.

6. We also detected concentrated emission at the velocity of about -100 km s^{-1} , corresponding to the "bar" in the $H\alpha$ speckle polarimetric observations of Falke et al. (1996).

7. For the three compact sources in the $H30\alpha$ images that correspond to the Weigelt blobs D, C and B we determined the proper motions to be about 6 mas yr^{-1} and their ejection epochs 1952.6, 1957.1 and 1967.6, respectively, close to the epochs of periastron passage.

8. The striking similarity between our images of the extended region, in the continuum and in the narrow $H30\alpha$ line, and those of the 345 GHz continuum and the emission line reported by Bordiu & Rizzo (2019) that they attributed to $\text{HCO}^+(4-3)$, led us to investigate the possibility that the observed line is instead a recombination line. The frequency of this line is indeed very close to that of the $H40\delta$ recombination line and, would in this case, be at a velocity of -64 km s^{-1} , which corresponds to the velocity of the NW extended emission region. Based on this identification, we modeled the compact regions detected in our observations and were able to reproduce the intensity of the line observed by Bordiu & Rizzo (2019), supporting our interpretation that this emission line is indeed $H40\delta$.

Future high-angular resolution observations using ALMA will be able to measure the proper motions of all the compact sources detected in this work, and also the effect of periastron passage on their continuum flux density and spectra.

6 DATA AVAILABILITY

The data underlying this article are available in ADS/JAO.ALMA#2017.1.00725.S

ACKNOWLEDGEMENTS

We would like to thank our referee, John Bally, for insightful comments that helped to improve this paper. This paper makes use of the following ALMA data: ADS/JAO.ALMA#2017.1.00725.S. ALMA is a partnership of ESO (representing its member states), NSF (USA) and NINS (Japan), together with NRC (Canada), MOST and ASIAA (Taiwan), and KASI (Republic of Korea), in cooperation with the Republic of Chile. The Joint ALMA Observatory is operated by ESO, AUI/NRAO and NAOJ. ZA and PPB acknowledge Brazilian agencies FAPESP (grant #2011/51676-9 and #2014/07460-0) and CNPq (grant #305768/2015-8)

REFERENCES

Abdala, H. and H.E.S.S. collaboration, 2020, *ã*, 633, 162
 Abraham, Z., Falceta-Gonçalves, D., Dominici, T. et al., 2005, *A&A*, 437, 977
 Abraham, Z., Falceta-Gonçalves, D., Beaklini, P.P. B., 2014, *ApJ*, 791, L95
 Abraham, Z., Falceta-Gonçalves, D., 2007, *MNRAS*, 378, 309
 Artigau, E., Martin, J. C., Humphreys, R. M., 2011, *AJ*, 141, 202
 Bordiu, C., Rizzo, J. R., 2019, *MNRAS*, 490, 1570
 Chesneau, O., Min, N., Herbst, T. et al., 2005, *A&A*, 435, 1043

Clementel, N., Madura, T. I., Cruip, C. J. H., Icke, V., Gull, T. R., 2014, *MNRAS*, 443, 2475
 Corcoran, M. F., Swank, J. H., Petre, R. et al., 2001, *ApJ*, 562, 1031
 Corcoran, M. F., Liburd, J., Morris, D., et al. 2017, *ApJ*, 838, 45
 Cox, P., Mezger, P.G., Sievers, A. et al., 1995a, *A&A*, 297, 168
 Cox, P., Martin-Pintado, J., Bachiller, R. et al., 1995b, *A&A*, 295, L39
 Damineli, A., 1996, *ApJ*, 460, L49
 Damineli, A., Stahl, O., Kaufer, A. et al., 1998, *A&AS*, 133, 299
 Damineli, A., Hillier, D. J., Corcoran, M. F. et al., 2008, *MNRAS*, 384, 1649
 Damineli, A., Fernández-Lajus, E., Almeida, L. A. et al., 2019, *MNRAS*, 484, 1325
 Davidson, K., Ebbets, D., Weigelt, G. et al., 1995, *AJ*, 109, 1784
 Davidson, K., Humphreys, R. M., 1997, *ARA&A*, 35, 1
 Davidson, K., Ebbets, D., Johansson, S. et al., 1997, *AJ*, 113, 335
 Davidson, K., Mehner, A., Humphreys, R. M., Martin, J. C., Ishibashi, K., 2015, *ApJ*, 801, L15
 Dorland, B. R., Currie, D. G., Hajian, A. R., 2004, *AJ*, 127, 1052
 Duncan, R. A., White, S. M., Lim, J. et al., 1995, *ApJ*, 441, L73
 Duncan, R. A., White, S. M., Lim, J., 1997, *MNRAS*, 290, 280
 Duncan, R. A., White, S. M., 2003, *MNRAS*, 338, 425
 Dwarkadas, V. V., Owocki, S. P., 2002, *ApJ*, 581, 1337
 Falceta-Gonçalves, D., Jatenco-Pereira, V., Abraham, Z., 2005, *MNRAS*, 357, 895
 Falke, H., Davidson, K., Hofmann, K.-H., Weigelt, G., 1996, *A&A*, 306, L17
 Gaviola, E., 1950, *ApJ*, 111, 408
 Gaviola, E., 1953, *ApJ*, 118, 234
 Groh, J. H., Madura, T. I., Hillier, D. J. et al., 2012, *ApJ*, 759, L2
 Gull, T. R., Vieira, G., Bruhweiler, K. E. et al., 2005, *ApJ*, 620, 442
 Gull, T. R., Kober, G. V., Nielsen, K. E., 2006, *ApJS*, 163, 173
 Gull, T. R., Nielsen, K. E., Corcoran, M. F. et al. 2009, *MNRAS*, 396, 1308
 Gull, T. R., Madura, T. I., Teodoro, M. et al., 2016, *MNRAS*, 462, 3196
 Hamaguchi, K., Corcoran, M. F., Pittard, J. M. et al. 2018, *Nature Astr.*, 2, 731
 Hamann, F., 2012, in *Eta Carinae and the Supernova Impostors*, ed. K. Davidson & R. M. Humphreys (Astrophysics and Space Science Library, Vol. 384, New York: Springer), 95
 Hillier, D. J., Davidson, K., Ishibashi, K., Gull, T., 2001, *ApJ*, 553, 837
 Hillier, D. J., Gull, T., Nielsen, K. et al., 2006, *ApJ*, 642, 1098
 Hartman, H., Damineli, A., Johansson, S. et al., 2005, *ã*, 436, 945
 Hofmann, K.-H., Weigelt, G., 1988, *A&A*, 203, L21
 Humphreys, R. M., Davidson, K., Smith, N., 1999, *PASP*, 111, 1124
 Hony, S., Dominik, C., Waters, L. B. F., M. et al., 2001, *A&A*, 377, L1
 Ishibashi, K., Gull, T. R., Davidson, K. et al., 2003, *AJ*, 125, 3222
 Johansson, S., Zethson, T., Harman, H. et al. 2000, *A&A*361, 977
 Johansson, S., Letokhov, V. S., 2001, *A&A*, 378, 266
 Johansson, S., Gull, T. R., Hartman, H., Letokhov, V. S., 2005, *A&A*, 435, 183
 Kiminki, M. M., Smithe, N., 2018, *MNRAS*, 477, 2068
 Martin, J. C., Davidson, K., Humphreys, R. M. et al., 2010, *ApJ*, 640, 474
 Mehner, A., Davidson, K., Ferland, G. J. et al., 2010, *ApJ*, 710, 729
 Morse, J. A., Davidson, K., Bally, J. et al., 1998, *AJ*, 116, 2443
 Morris, P. W., Waters, L. B. F. M., Barlow, J. M. et al., 1999, *Nature*, 402, 50
 Morris, P.W., Gull, T.R., Hillier, D.J. et al., 2017, *ApJ*, 842, 79
 Natta, Natta, A., Giovanardi, C., 1991, in *The Physics of Star Formation and Early Stellar Evolution*, ed. C. J. Lada D. D.
 Nielsen, K. E., Gull, T. R., Kober, G. V., 2005, *ApJS*, 157, 138
 Nielsen, K. E., Corcoran, M. F., Gull, T. R. et al., 2007, *ApJ*, 660, 669
 Panagia, N., Felli, M., 1975, *A&A*, 39, 1
 Parkin, E. R., Pittard, J. M., Corcoran, Hamaguchi, K. 2011, *ApJ*, 726, 105
 Rebollo, D., Burton, M., Green, A. et al. 2016, *MNRAS*, 456, 2406
 Reitberger, K., Reimer, A., Reimer, O., Takahashi, H., 2015, *ã*, 577, 100
 Remmen, G.N., Davidson, K., Mehner, A. 2013, *ApJ*, 773, 27
 Russell, C. M., Corcoran, M. F., Hamaguchi, K. et al. 2016, *MNRAS*, 458, 2275
 Smith, N., Gehrz, R. D., Krautter, J., 1998, *AJ*, 116, 1332

- Smith, N., Gehrz, R. D., Hinz, P. M. et al., 2003a, *AJ*, 125, 1458
Smith, N., Davidson, K., Gull, T., Ishibashi, K., Hillier, D. J., 2003b, *ApJ*, 586, 432
Smith, N., 2004, *MNRAS*, 351, L15
Smith, N., Morse, J. A., Gull, T. R. et al., 2004, *ApJ*, 605, 405
Smith, N. 2005, *MNRAS*, 357, 1330
Smith, N., Ginsburg, A., Bally, J., 2018, *MNRAS*, 474, 4988
Steiner, J. E., Daminieli, A., 2004, *ApJ*, 612, L133
Storey, P.J., Hummer, D.G. 1995, *MNRAS*, 272, 41
Teodoro, M., Daminieli, A., Sharp, R.G., Groh, J.H., Barbosa, C.L., 2008, *MNRAS*, 387, 564
Teodoro M., Daminieli A., Heathcote B., Richardson N. D., Moffat A. F. J., 2016, *ApJ*, 819, 131
Verner, E.M., Gull, T. R., Bruhweiler, F., et al., 2002, *ApJ*, 581, 1167
Verner, E.M., Bruhweiler, F., Gull, T., 2005, *ApJ*, 624, 973
Weigelt, G., Ebersberger, J., 1986, *A&A*, 163, L5
Weigelt, G., Albrecht, R., Barbieri, C. et al., 1995, *Revista Maxicana de Astronomia y Astrofísica Serie de Conferencias*, Vol. 2 (ed. Niemela, V., Morrel, N., Feinstein, A.), 11
Weigelt, G., Kraus, S., 2012, in *Eta Carinae and the Supernova Impostors*, ed. K. Davidson & R. M. Hunphreys (*Astrophysics and Space Science Library*, Vol. 384, New York: Springer), 129
Weigelt, G., Hofmann, K.-H., Schert, D., Clementel, N., Corcoran, M. F. et al., 2016, *A&A*, 594, 106
White, S.M., Duncan, R.A., Lim, J. et al., 1994, *ApJ*, 429, 380
Zanella, R., Wolf, B., Stahl, O. 1984, *A&A*, 137, 79

This paper has been typeset from a $\text{\TeX}/\text{\LaTeX}$ file prepared by the author.